Catena 207 (2021) 105689

Contents lists available at ScienceDirect

Catena

journal homepage: www.elsevier.com/locate/catena

Palaeoenvironmental changes in the Iberian central system during the Late-glacial and Holocene as inferred from geochemical data: A case study of the Navamuño depression in western Spain

Valentí Turu [a,b,*], Rosa M. Carrasco [a], José Antonio López-Sáez [c], Xabier Pontevedra-Pombal [d], Javier Pedraza [e], Reyes Luelmo-Lautenschlaeger [c,f], Sebastián Pérez-Díaz [g], Anna Echeverria-Moreno [b], Jaime Frigola [h], Francisca Alba-Sánchez [i], Jesús Sánchez-Vizcaíno [b], Albert Pèlachs-Mañosa [j], Raquel Cunill-Artigas [j], Jordi Nadal-Tersa [j], Elena Mur-Cacuho [j], Joan Manuel Soriano-López [j]

[a] Department of Geological Engineering and Mining, University of Castilla-La Mancha, Avda. Carlos III s/n, 45071 Toledo, Spain
[b] Fundació Marcel Chevallier, Edifici Socio-Cultural de la Llacuna, AD500 Andorra la Vella, Andorra
[c] Environmental Archaeology Research Group, Institute of History, CSIC, Albasanz 26-28, 28037 Madrid, Spain
[d] Dpto. Edafoloxía e Química Agrícola, Fac. Bioloxía, Universidade de Santiago de Compostela, Lópe Gómez de Marzoa s/n, Campus Vida, 15782 Santiago de Compostela, Spain
[e] Department of Geodynamics, Stratigraphy and Palaeontology, Complutense University, José Antonio Novais 12, 28040 Madrid, Spain
[f] Department of Geography, Autonoma University of Madrid, C/Francisco Tomás y Valiente 1, Campus de Cantoblanco, 28049 Madrid, Spain
[g] Department of Geography, Urban and Regional Planning, University of Cantabria, Avda. de los Castros s/n, 39005 Santander, Spain
[h] CRG Marine Geosciences, Department of Earth and Ocean Dynamics, University of Barcelona, 08028 Barcelona, Spain
[i] Department of Botany, University of Granada, 18071 Granada, Spain
[j] Department of Geography Autonoma University of Barcelona (Grup de Recerca en Àrees de Muntanya i Paisatge, GRAMP), Edifici B. Fac. Filosofia i Lletres, 08193 Bellaterra (Cerdanyola del Vallés), Barcelona, Spain

ARTICLE INFO

Keywords:
Late Glacial
Holocene
Geochemistry
Palaeoclimate
Dust-Ashs-Aerosols

ABSTRACT

The Iberian Central System (ICS) is a clue region to reveal Mediterranean/Atlantic inferences over Iberia. We present a multidisciplinary study from western Spain conducted in the Navamuño depression (ND), covering the last 16.8 ka (cal BP). A reconstruction of the palaeotemperature from the resulting geochemical data highlights four cold and dry intervals, namely, the Oldest Dryas, Older Dryas, Intra-Allerød Cold Period (IACP), and the Younger Dryas, along with warmer intervals: the Bølling (14.7–14 ka) and the Allerød (12.9–12.6 ka); however, the Greenland Interstadial GI-1c (13.4–13.1 ka) is barely distinguishable in the ND. Despite the shortage of biomass to sustain fire, the earliest charcoals are from ~14.4–13.8 ka. Evidence of ash/dust events overprinting the geochemical background starts at ~13.8–12.8 ka. Significant fire activity in the Early Holocene at ~11.7–10.6 ka affected the ND, matching the westernmost ICS data. This period includes short oceanic spells inferred from Cl peaks at ~10.9–10.2 ka and three cold intervals at 11.4, 9.3, and 8.2 ka disrupted the progressive temperature increase. The Mid-Holocene showed a continuously increasing trend towards an arid climate, peaking at 4.2 ka under a pervasive dust influx from North Africa, which has prevailed since almost ~7.9 ka. A prominent volcanic event at ~6.8–5.8 ka is in Navamuño and Roñanzas (Asturias, N Spain; Gallego et al., 2013) identified from heavy metal-rich layer, synchronous with the last known eruption of the Calatrava volcanic field (South-Central Spain; Poblete-Piedrabuena et al., 2019). This volcanic eruption could affect many other regions half north of Iberia. The pervasive presence of oceanic aerosols in the last three millennia (2.8 ka ~) allowed the formation of a Cl-rich peat layer during the Ibero-Roman humid period ~2.1 ka, before a changing around ~0.4 ka toward colder and drier conditions at the Little Ice Age (LIA) period.

* Corresponding author at: Department of Geological Engineering and Mining, University of Castilla-La Mancha, Avda. Carlos III s/n, 45071 Toledo, Spain.
E-mail address: vturu@andorra.ad (V. Turu).

https://doi.org/10.1016/j.catena.2021.105689
Received 19 September 2020; Received in revised form 15 August 2021; Accepted 18 August 2021
Available online 2 September 2021

1. Introduction

The 'last termination' refers to the warm period between the last glacial maximum (LGM) and the onset of the Holocene (~11.7 ka cal BP). Proxy studies reveal multi-phase deglaciation in SW Europe (Allard et al., 2021) and are linked to distant climate teleconnections (Turu, 2018). A general warming trend is observed during the deglaciation, disrupted by some cold and generally arid stadials that affected the extent of ice sheets and valley glaciers (Fletcher et al., 2010). Deglaciation studies have primarily focused on moraines or other geomorphologically related deposits using absolute dates and trying to fit the corresponding climate (Carrasco et al., 2013, 2015a; Vieira et al., 2021; Allard et al., 2021 and references therein). In contrast to the northern Iberia (González-Sampériz et al., 2006; Jalut et al., 2010) in the central Iberian mountains, a limited number of long (>11 ka cal BP) and continuous terrestrial sedimentary records have been described by van der Knaap and van Leeuwen, 1994, 1995, 1997; Connor et al., 2012; Turu et al., 2018; López-Sáez et al., 2020). However, significant progress in studying glacial phases and peat-based palaeoenvironments has allowed the reconstruction of Holocene vegetation dynamics (Morales-Molino et al., 2013; López-Sáez et al. 2014, 2020 and references therein). However, these studies lacked detailed geochemical analyses. In this study, we present the results of palaeoenvironmental research based on geochemistry investigating the sedimentary record of Navamuño over the last 16 ka (16339–16800 yr cal BP; Turu et al., 2018). The primary purpose of this study was to determine the lenitic-catchment history during the deglaciation in the western Iberian Central System (ICS) by analysing the geochemical elements and the magnetic susceptibility (MS) of the deposits. Previous studies that have considered this site (Carrasco et al., 2008, 2013, 2015a, 2015b, 2018; Turu et al., 2018; López-Sáez et al., 2020) have shown this sequence to be a potentially continuous archive (on a millennial to centennial-scale) of the regional hydrological insights over the last 16 millennia. We also present an improved, robust chronological model that builds on previously published data (Turu et al., 2018). In addition, the sequence also indicates the pervasive influences of episodic dust and ash comming from distant areas. Calcite-rich dust from Asia (Fitzgerald et al., 2015) or K/Na-aluminosilicates dust from North Africa thorughly sea-spray cloud-processed on the way to Europe (Fitzgerald et al., 2015) affected the Navamuño's geochemical background. Saharan dust (SD) particles transported to Europe show a noticeable accumulation of S (Dall'Osto et al., 2010) since African particles reacts readily in the presence of sulfates (Fitzgerald et al., 2015). Overprinted onto dusty episodes (Oppenheimer, 2003), particles from volcanic eruptions may also exist in this region. Notably, only a few Iberian continental records have focused on this aspect, and our study aims to fill this gap.

2. Study area

Located in the Sierra de Béjar (Western Iberia), the Navamuño depression (ND) consists of a pseudo-endorheic (~30 ha) intramountain graben that overlies a granitic bedrock from the western sector of the Sierra de Gredos mountain range (ICS). The continental environment (Köppen-Geiger Climate Classification Dsb and DsC; AEMET & IPMA, 2011) strongly influenced the area; however, drought generally occurs during the summer as in many Mediterranean climate areas, with intense rainfall occurring in autumn and winter. The region is influenced by the southwestern Atlantic depression and is dominated by synoptic anticyclones under the Azores High. The average annual rainfall on the Béjar Mountains ranges between 800 mm and 1000 mm, with higher precipitation at the summits (~2000 mm). The mean annual temperature is 9.5 °C (Durán et al., 2013), and the temperature oscillates between −4 °C and 3 °C in winter and varies between 22 °C and 32 °C in summer.

Recent studies (Carrasco et al., 2018) have shown that ND had a complex evolutionary history associated with former glacial processes (Turu et al., 2018; Carrasco et al., 2018) markedly affected the current morphology and sedimentary infill.

The depressions in the area formed mainly during the early stages of the ICS due to the tectonic reactivation of an intraplate mountain during the Miocene (Pedraza, 1994; de Vicente et al., 2011). The subsidence of some of these basins ceased in the Quaternary. However, the ND continued to subside with more significant infill than in other basins of the ICS, which were mainly associated with the Cuerpo de Hombre (CH) glacier (Fig. 1; Turu et al., 2018; Carrasco et al., 2018). The following three essential elements define the morphology of the ND.

A. Structural granite slopes form the northern, southern, and western boundaries of the depression.
B. The border moraine of the Cuerpo de Hombre (CH) glacier forms the eastern boundary of the depression, denoted as 'the principal moraine' by Pedraza et al. (2013).
C. The current meadows on the bottom plain (Fig. 1) were originally generated as moraine-dammed ponds.

3. Rationale

Mid-latitude palaeoenvironmental and palaeohydrological reconstructions at the millennial scale are crucial for understanding the Western Mediterranean climate-sensitive environmental evolution, which has been subjected to permanent climate connections between the high and low latitudes (Morellón et al., 2009; Fletcher et al., 2010). However, the availability of continuous high-resolution archives is limited and often includes insufficient dates and inherent uncertainties (Zielhofer et al., 2017a).

The core from Navamuño provides a continental record of the entire Late Glacial–Holocene period in the ICS (López-Sáez et al., 2014; Turu et al., 2018). A complete geochemical study has allowed us to understand the local and extra-basin sedimentary influx and compare the results with those of other sites in Iberia. Evidence of volcanic and dust influx, which was identified from geochemical data, can be found in Roñanzas (Fig. 1; Asturias, northern Spain), in Lake Redon (Fig. 1; Central Pyrenees) and some indices in Villarquemado (Fig. 1; Iberian Range). This study investigated the following aspects:

1) Are the geochemical data sufficient to be able to reconstruct the Holocene palaeoclimate in Navamuño?
2) When was Navamuño under the influence of global atmospheric episodes?
3) How does the oceanic climate influence Navamuño and when?

4. Materials and methods

Sediment geochemistry, environmental magnetism, and a range of sedimentological properties provide compelling information about the factors and processes within watersheds characterised by lenitic ecosystems such as lakes and endorheic basins. These factors and processes include the strength of sediment fluxes, the rate at which atmospheric dust is deposited, fires, climate variability, and depositional processes that ultimately control sediment accumulation patterns and biogeochemical characteristics (Koinig et al., 2003; Kylander et al., 2011; Magny et al., 2013).

4.1. Sedimentology, bulk geochemical composition, and statistical analysis

Field descriptions of the materials and MS measurements (Turu et al., 2018) were initially used to investigate the nature of the sediments (Fig. 2). The cores were split into two, and one half was hermetically sealed at a constant temperature at the Department of Geodynamics, Stratigraphy, and Palaeontology in the Complutense University of Madrid for future study. The other half was transferred to the CORELAB

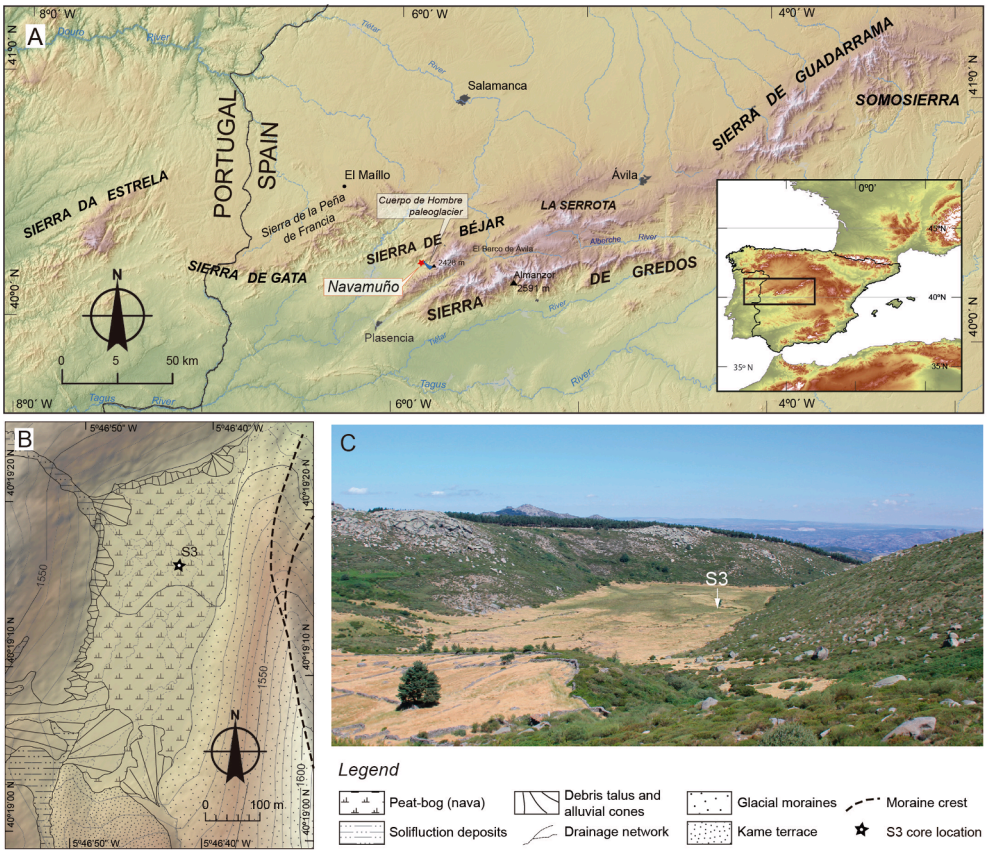

Fig. 1. Location of Navamuño within the western Iberian Central System (A); geomorphological scheme of the Navamuño depression or N*ava* and the cored zone is indicated (B); general view of the *Nava* from the southwest (C).

laboratory at the University of Barcelona to acquire high-resolution images and luminosity using a colour line scan camera on an Avaatech XRF (X-ray Fluorescence) core scanner. These samples were also analysed using an XRF core scanner for semi-quantitative determination (Richter et al., 2006; Croudace et al., 2019) of the abundances of the chemical elements determined by counts (CTS; Fig. 3). Two read-time spectrums of intensity and voltage were obtained by a centimetric (1 cm) measurement sequence of 10-s reading-time using 0.6 mA at 10 kV AC to detect the low atomic weight elements (Al to Co), and 40-s reading-time sequence using 1.3 mA at 30 kV AC with a Pd filter, to measure higher atomic weighted elements (Ni and Pb).

Palaeoenvironmental interpretations were made using the raw data obtained from the XRF analysis while avoiding the use of scale effects should preferably be avoided and average values obtained from centred distributions (Eriksson et al., 1999). The relative elemental ratios were normalised for the average values of the entire core divided by the standard deviation (Z-score). These data were used for principal component analysis (PCA) to study the variance–covariance (Hammer et al., 2001) by using PAST software (v.3). Treating the data in this manner (727 samples) allowed us to obtain groups of representative elements that follow similar tendencies (Figs. 4 and 5). After selecting the palaeoenvironmental and statistically significant elements, we obtained the Spearman's rank correlation coefficient used for the statistical analysis (Table 3).

The results of PCA (component 1; Figs. 4–6) support the idea that Al, Ti, Fe, Zr, Rb, Si, and K have a common origin, probably related to weathering of silicates (clays and quartz) in the occurrence of secondary minerals (Morellón et al., 2009; Oliva-Urcía et al., 2018); indicating the highest loadings of K and Si in the two-phase component of higher sedimentary loads (López-Merino et al., 2010; Haliuc et al., 2017; Oliva-Urcía et al., 2018). Notably, Fe and Mn, mainly influenced by redox conditions, are considered principal components (Figs. 4–5). The presence of Fe in many primary and secondary minerals (e.g. oxides and hydroxides), apart from silicates (Mackereth, 1966; Schaller et al., 1997), suggests that it is prevalent. Variations in PC1 may reflect changes in the mineral assemblages. At the same time, the positive direction of PC2 suggests a detrital input, which may be related to the processes that affect the catchment, such as runoff regime, active tectonics (Carrasco et al., 2018), vegetation cover, soil changes (Haliuc et al., 2017), and dust/ash rain events (Le Roux et al., 2012; Gallego et al., 2013).

The ratio of chemical elements was used to interpret the sedimentary environment (geological condition) or the climatic conditions under which it formed (environmental conditions) (Calvert and Pedersen, 2007). The Al/Ti ratio characterises terrigenous components over time in both non-carbonated lake-like systems (López et al., 2006; Schröder et al., 2018) or in karstified lake-like systems (Hôbig et al., 2012). Therefore, in the ND, Al^{+3} can be used as an efficient tracer of extreme acidic media (pH < 4), and Ti can be used as an efficient tracer of energy transportation because of its high density (Turu and Bordonau, 2013). The Ti indicates that mechanical erosive processes took place in the basin (Höbig et al., 2012). It may derive from the physical erosion of Ti-bearing rocks (Cohen, 2003) because minerals containing Ti are insensitive to dissolution (Demory et al., 2005). However, other sources for Ti is not discarded and is discussed further down on the text. The redox-sensitive minerals containing manganese (Mn) and iron (Fe) can react to geochemical changes in the depositional environment; therefore, the Mn/Fe ratio is considered as a proxy for former redox conditions (Koinig et al., 2003). The Mn is highly insoluble under oxygenated conditions; hence elevated Mn/Fe ratios depict an oxygen-rich environment, whereas low Mn/Fe ratios reflect a more anoxic environment at the water/sediment interface.

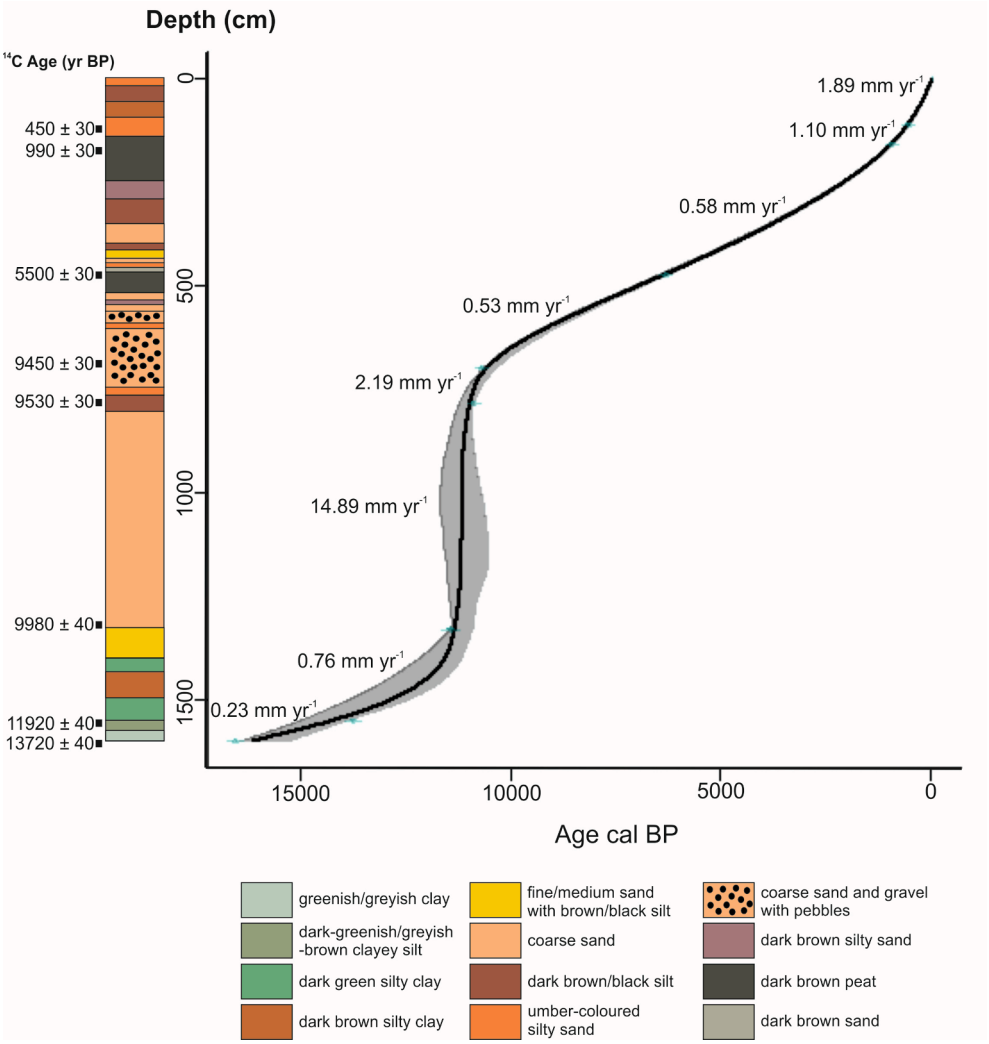

Fig. 2. Simplified lithostratigraphy and age model. Samples providing the AMS and calibrated ^{14}C ages (blue points) are listed in Table 1. The model (smooth spline 0.2, black line) considers the 2σ-confidence range of calibrated ages (grey areas). Sediment accumulation rates (mm yr^{-1}) are shown between individual radiocarbon ages. (For interpretation of the references to colour in this figure legend, the reader is referred to the web version of this article.)

The deposit's host minerals can be identified based on the grain size and subsequent particle size sorting within the sediments (Koinig et al., 2003; Haliuc et al., 2017). Ti, Rb, and K are often associated with mineral assemblages, while Zr and Si are linked to fractions containing coarser particle-size of silt and sandy fractions (Kylander et al., 2011). Increases in LOI (bulk organic matter content) and the lithogenic element-assemblages are inversely correlated in the ND, inferred from principal components PC1 and PC2 (Fig. 6).

4.2. Core sampling, accelerator mass spectrometry dating, age-depth model, and probability of events

The basin infill architecture was firmly established using the sequential stratigraphy method (Catuneanu, 2006; Turu et al., 2007; Turu et al., 2017, 2018) to the geophysical data produced in the ND (Carrasco et al., 2018). Currently, the hydrological dynamics in this region correspond to those of a bogland. Turu et al. (2018) performed the facies analysis, sampling, dates, MS, LOI, and charcoal counting in sediments from a borehole extracted from the middle of the northern sector of the ND in 2015. The ages of the samples (from dating analysis) (Table 1) were obtained from the Beta Analytic Inc. (Miami, USA) accelerator mass spectrometry (AMS) facility. Results were provided as calibrated ages according to the INTCAL13 curve (Reimer et al., 2013). The samples used for AMS analysis were mainly from palaeosoils embedded within sandy layers (Turu et al., 2018). Beneath these layers, silty-clay sediments extend to the deepest part of the borehole. López-Sáez et al. (2020) performed the Late Glacial palynology of the core, although pollen analysis from the fibric-rich units (following the Van Post criteria) of the middle and upper Holocene remains unpublished. Considering the chronological uncertainties (Blaauw et al., 2007), a refined age-depth model was applied using the Clam 2.2 software (Blaauw, 2010), based on the R Foundation for statistical computing application package (Fig. 2) for the Holocene (Turu et al., 2018) and the Upper Pleistocene strata (López-Sáez et al., 2020).

Major stratigraphic boundaries (Fig. 3) and probabilities (Turu et al., 2018) for the middle and lower part of the Holocene are shown in Fig. 3 (and Supplementary Appendix A1). The Bacon R v2.2 software (Blaauw et al., 2010) estimates the event probabilities by detecting specific proxy features such as the rising values of a proxy or its decrease. Event probabilities (or the probability of an event) were calculated over specific periods (see Supplementary Appendix A1). Also, comparisons of sedimentary rates (Fig. 2) from those from the ICS are available (see Supplementary Appendix A2) and typically range from 0.43 mm/yr – 0.23 mm/yr.

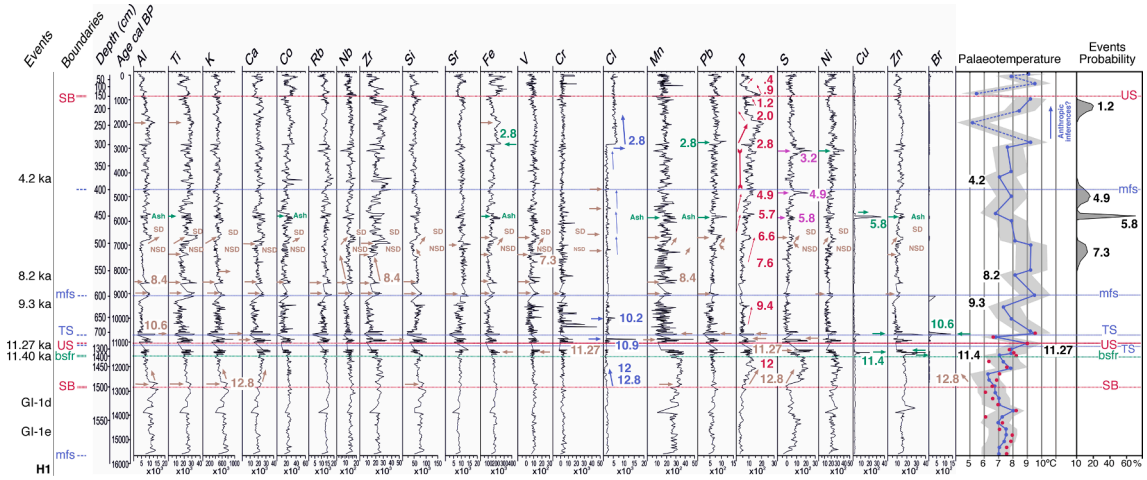

Fig. 3. Geochemical stratigraphy of the most significant chemical elements of Navamuño core plotted against age (cal BP). Arrows show switching behaviours or trends of elements. Coloured numbers are ages in ka cal BP, for heavy metals significance (in green), phosphorous (in red), chlorine (in blue) or Al and Ca-rich silicates (in brown). Brown letters are from Saharan dust (SD) or Non-Saharan dust (NSD) influx (see main text). Colour lines are unconformities (US: unconformity surface), stratigraphical surfaces (SB, surface boundary), facies assemblages (TS, transgressive surface; bsfr: the basal surface of forced regression; mfs: maximum flooding surface). To the right of the figure corresponds to the probability of an event peaking at 7.3, 5.8, 4.9, 1.2 ka cal BP, mentioned in the main text. Also computed palaeotemperatures plotted as blue dots, overprinted (red dots) data from López-Sáez et al. (2020). To the left of the figure: climate events mentioned in the main text. Portions of low resolution within the core were removed, indicated as a gap (only in the Cu column to facilitate the lecture of the figure). (For interpretation of the references to colour in this figure legend, the reader is referred to the web version of this article.)

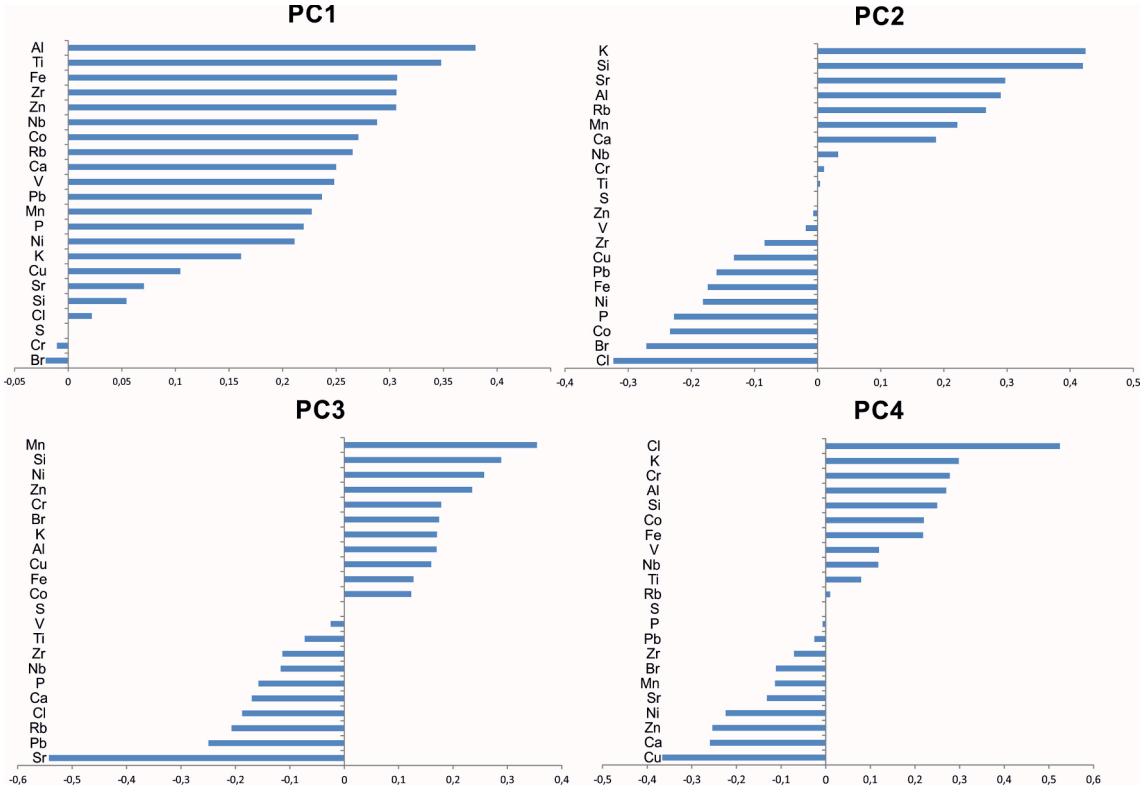

Fig. 4. Loadings of the analyzed geochemical elements on the Principal Components obtained by PCA analysis.

4.3. Loss-on-ignition, magnetic susceptibility, sedimentary macro-charcoal analysis and sedimentary rates

The weight lost from samples that were obtained from organic-rich layers upon ignition is a valuable technique for identifying the palaeovegetation production based on the sample remains (Pèlachs et al., 2011; Turu et al., 2018). Because the presence of moisture would produce a relative result, the sample must be dried firstly. Thus, the samples were heated to 105 °C in a ventilated oven and weighed. The samples were again heated to 550 °C to combust all the organic matter in the samples and weighed again. The difference between these weights is the LOI, expressed as a percentage (Heiri et al., 2001).

Measuring the MS of both rocks and sediments is helpful because it provides mineralogical information (Thompson and Oldfield, 1986). In the case of sediments, MS can provide information regarding their place of origin. MS can also provide information on diamagnetic properties of

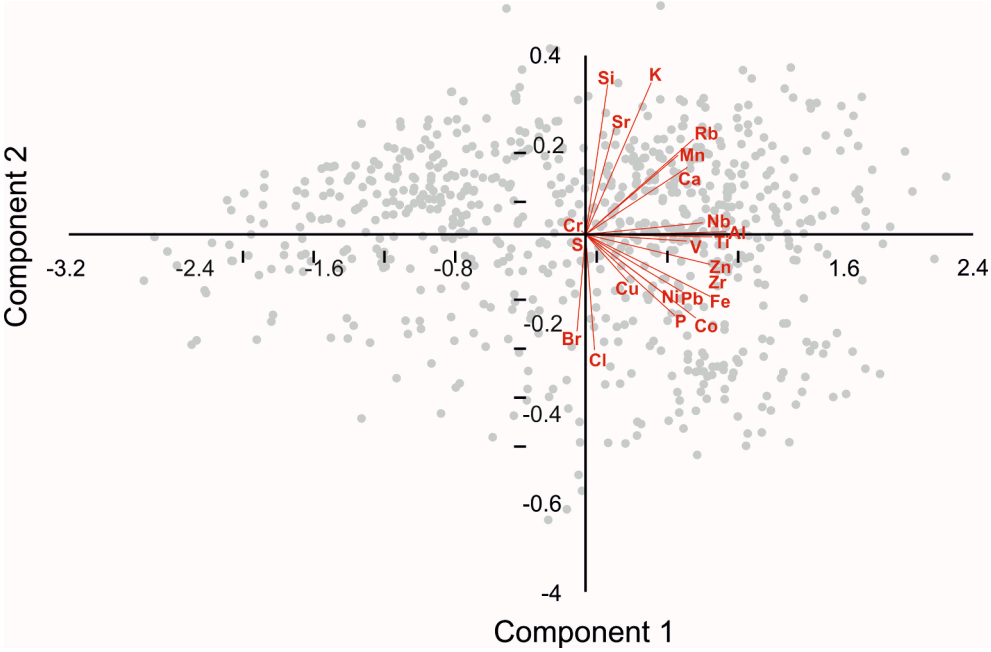

Fig. 5. PCA double plot of vectors (red) represents geochemical elements and samples (grey circles) on the first two principal component axes. (For interpretation of the references to colour in this figure legend, the reader is referred to the web version of this article.)

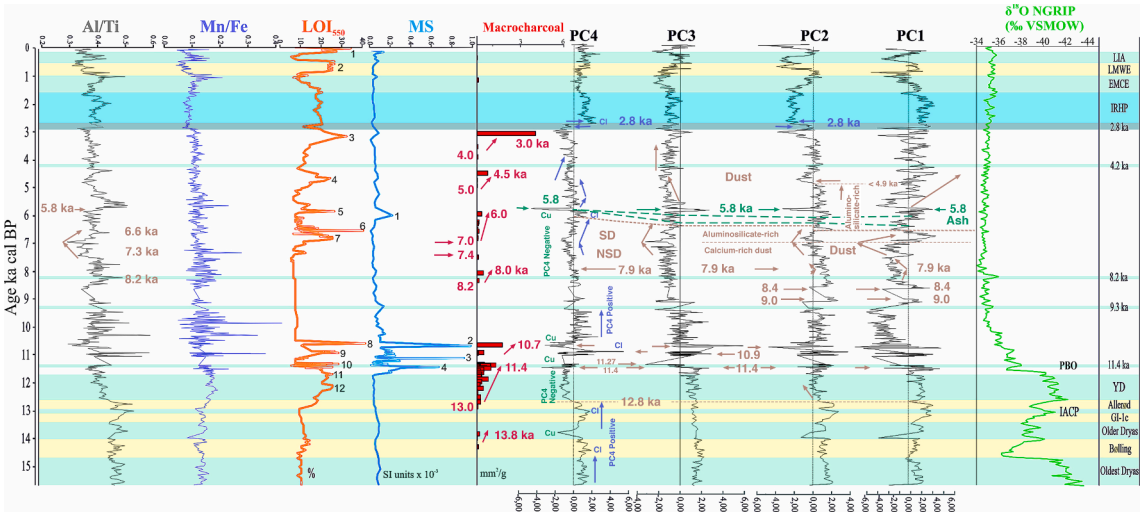

Fig. 6. Selected geochemical ratios, LOI, magnetic susceptibility (MS), macro-charcoals and principal components derived from PCA analysis of Navamuño record, and δ18 O record from NGRIP record (Rasmussen et al., 2008, 2014) plotted against age (cal BP). Colour shading corresponds to climatic events mentioned in the text: YD (Younger Dryas), IRHP (Ibero-Roman Humid Period), EMCE (Early Medieval Cold Episode), LMWE (Late Medieval Warm Episode), LIA (Little Ice Age). The figure also shows LOI (1 to 2; >20%) and MS (1 to 4; >0.2SI units) peaks. Coloured numbers are ages in ka cal BP, for significant Cu (in green), charcoals (in red), chlorine (in blue) or Al and Ca-rich silicates (in brown). Brown letters are from Saharan dust (SD) or Non-Saharan dust (NSD) influx; see main text. Arrows show switching PCA behaviours or trends. (For interpretation of the references to colour in this figure legend, the reader is referred to the web version of this article.)

Table 1
AMS and calibrated ^{14}C ages for the core sequence from Navamuño, western Iberian Central System, Spain.

Lab code	Depth (cm)	Material dated	δ^{13}C (‰)	^{14}C Age BP	Calibrated range (cal BP)	Median probability (cal BP)
ß-409998	111	Sedge seeds	−26.8	450 ± 30	535–472	509
ß-409997	159	Bulk	−25.7	990 ± 30	961–798	913
ß-409999	475	Sedge seeds	−26.8	5500 ± 30	6395–6217	6298
ß-410000	700	Sedge seeds	−25.9	9450 ± 30	10754–10587	10686
ß-410001	785	Sedge seeds	−27.9	9530 ± 30	11072–10707	10868
ß-410003	1330	Bulk	−26.9	9980 ± 40	11619–11264	11426
ß-410004	1550	Sedge seeds	−29.3	11920 ± 40	13942–13568	13744
ß-412870	1600	Bulk	−25.5	13720 ± 40	16800–16339	16561

palaeosoils, their ferromagnetic properties of weathered products, carbonate and iron leaching, ash horizons and charred matter that results from burning events. MS also informs about paramagnetic products originating from anthropogenic activity (ore prospecting, mining, burnings, pavements, and paths). The use of MS data with apophyte allows human-induced impacts to be distinguished against natural processes. Unfortunately, apophytes are not available since the palynology of the Holocene remains unpublished. The relative simplicity and usefulness of MS measurements have led to its widespread use. The ND samples were subjected to MS measurement (Turu et al., 2018) using a passband of 3 ± 0.5 cm and an overlap of 6 ± 1 cm, using an SM-20 device from GF Instruments (Czech Republic) (Fig. 6).

Macro-charcoal counting provides valid results in palaeoenvironmental studies (Bal et al., 2011), and it has been applied in the ND by Turu et al. (2018). Sampling followed steps of 1 cm intervals alternating the material for the macro-charcoal counting (Turu et al., 2018) and pollen identification, and the last was performed by López-Sáez et al. (2020) for the oldest part of the sequence. After sieving with a 0.15-mm mesh, macro-charcoal counting was performed every 0.0625 mm^2 (over a total area of 6.25 mm^2). We used 1-g samples to minimise the effect of suing samples of different densities (Carcaillet et al., 2007). The samples were pre-treated with KOH as a flocculant and 15 % NaCl to dissolve any organic material (Finsinger et al., 2014). The results from macro-charcoal counting are in mm^2/g (Fig. 6) given.

4.4. Phosphorus content as a proxy

P content is a climate proxy for glaciated areas (Kjær et al., 2015) and is primarily linked to glacier fluctuations in cold periods (Hodson, 2008). The P content in related soils and sediments was high during the LGM, as in other cold periods, while it was ten times lower in the warmer periods of the last glacial cycle (Kjær et al., 2015). Since P concentrations are negatively correlated with temperature, in the same manner as deuterium excess (δD) and $\delta^{18}O$ (Kjær et al., 2015), it can be used as a palaeothermometer when calibrated in situ. We, therefore, used the palaeotemperatures obtained by López-Sáez et al. (2020) from the Late Glacial period for calibration (Supplementary Appendix A3). In the core, P determinations from comparable samples in density or compaction are suited. The P-computed palaeotemperatures were found to fit these independent data (Fig. 3). Tentatively, its projection onto the Holocene can therefore transduce the geochemistry data into a quantitative palaeoclimate proxy (Fig. 3).

5. Results

The analysed core spans the last ~15.6 ka cal BP years (Table 1). The lowest part of the core between ~16.8–15.6 ka cal BP was sacriffied for AMS dates and geomechanical testing (Turu et al., 2018). The radiocarbon dates follow the stratigraphic order (Table 1) without any significant hiatus. From these data, we could produce and an age-depth model (Fig. 2). The bulk $\delta^{13}C$ values in the analysed samples mainly range from −25.5 ‰ to −29.3 ‰ (Table 1), indicating the presence of terrestrial C3-type plants (Deines, 1980); no ageing effect was observed (Turney et al., 2000), and the samples come from different organic sources (Table 1). A low sedimentation rate (~0.23–0.76 mm/yr) is between 1586 cm (bottom of the core) and 1330 cm depth, while higher values (~14.89 mm/yr) are achieved between 1330 cm and 785 cm. The sedimentation rate then stabilises (~2.19 mm/yr) between 785 cm and 707 cm (Fig. 2) and remains relatively constant (0.53–0.58 mm/yr) between 700 cm and 159 cm, increasing exponentially (1.10–1.89 mm/yr) towards the top of the core (Fig. 2). Nevertheless, the upper and lower boundaries range from 0.13 mm/yr to 1.23 mm/yr in the ICS (see Supplementary Appendix A2). Rapid changes in the sedimentary rate, such as those between 1330 cm and 785 cm, corresponding to a period of disturbance (Ko≥aczek et al., 2018) that occurred between the stratigraphic boundaries (Carrasco et al., 2018) and hiatuses (Turu et al., 2018). All anthropogenically disturbed zone (Fia≥kiewicz-Kozie≥ et al., 2015) are restrained to the upper 0.5 m of the core. Nevertheless, the aforementioned model follows a continuous curve without any significant hiatus.

The sedimentary profile of the Navamuño sequence (Turu et al., 2018) shows many fine grain-size facies (clay, clayey silt, silty clay, silt, silty sand, peat) and textures, including sands with gravels and pebbles (753–605 cm and 593–558 cm). A remarkable stratum covering almost 5 m is composed exclusively of coarse sands between 1330 cm and 803 cm, representing a short period in the ND sequence. A simplified stratigraphy of the sequence is presented in Table 2 and shown in Fig. 2.

The high-resolution record of the geochemical elements obtained using the XRF core scanner is shown in Fig. 3. Their variations in the elemental composition are summarised in four principal components (Figs. 4–5), which explain 62.58 % of the total variability. PC1 explains 33.68 % of the variance (Fig. 6), with Al, Ti, Fe, Zr, and Zn showing high positive loadings (>0.3); Nb, Co, Rb, Ca, V, Pb, Mn, P, and Ni have a moderately positive loading (>0.2 and < 0.3); K, Cu, Sr, Si, Cl, and S show low positive loadings (<0.2), and Cr and Br have low negative factor loadings in this component. The high positive loadings of the lithogenic elements (Al, Ti, Fe, and Zr) are indicative of the significant amount of fine/coarse-grained mineral matter (clay mineral assemblages) in the core sediments (Abel-Schaad et al., 2018). While Ti is generally associated with fine-grained minerals, Zr is usually associated with coarser minerals (Taboada et al., 2006). Thus, the joint appearance of these elements indicates the non-selective process by which mineral matter reached the ND sediments. However, a similar distant origin for these element assemblages is presented in the following sections. Pb and Nd were used to identify the source of dust/ash at Etang La Gruère (Switzerland) by Le Roux et al. (2012) (Fig. 7a), while Gallego et al. (2013) did the same but using V and Hg content at Roñanzas (Asturias, Northern Spain) (Fig. 7a). Nevertheless, PC2 captures 13.39 % of the total variance, mainly represented by K and Si (>0.4) with very high positive loadings. Sr and Al also show high loadings (>0.3 to < 0.4); Rb,

Table 2
Simplified stratigraphic description of the Navamuño sequence.

Depth (cm)	Stratigraphic description
12–1	Light umber-coloured silty sand with abundant plant debris
50–12	Dark brown silt
86–50	Dark brown silty clay
135–86	Light umber-coloured silty sand
254–135	Dark brown peat with abundant plant debris
292–254	Dark brown silty sand
350–292	Dark brown silt with some plant debris
392–350	Coarse sand
414–392	Dark brown silt with some plant debris
435–414	Fine sand with brown/black silt
442–435	Coarse sand
456–442	Light umber-coloured silty sand
465–456	Dark brown sand with plant debris and charred materials
512–465	Dark brown peat
525–512	Coarse sand
531–525	Dark brown silty sand
558–531	Coarse sand
593–558	Coarse sand and gravels with pebbles
605–593	Light umber-coloured silty sand
753–605	Coarse sand and gravels with pebbles with some plant debris
758–753	Light umber-coloured silty sand
803–758	Dark brown silt with some plant debris
1330–803	Coarse sand
1400–1330	Medium sand with dark brown silt with macro-charcoals and charred materials
1420–1400	Dark green silty clay
1495–1420	Dark brown silty clay with some plant debris
1542–1495	Dark green silty clay
1576–1542	Dark-greenish/greyish-brown clayey silt
1581–1576	Greyish clay
1590–1581	Greenish-grey clay
1600–1590	Bluish silts and clays

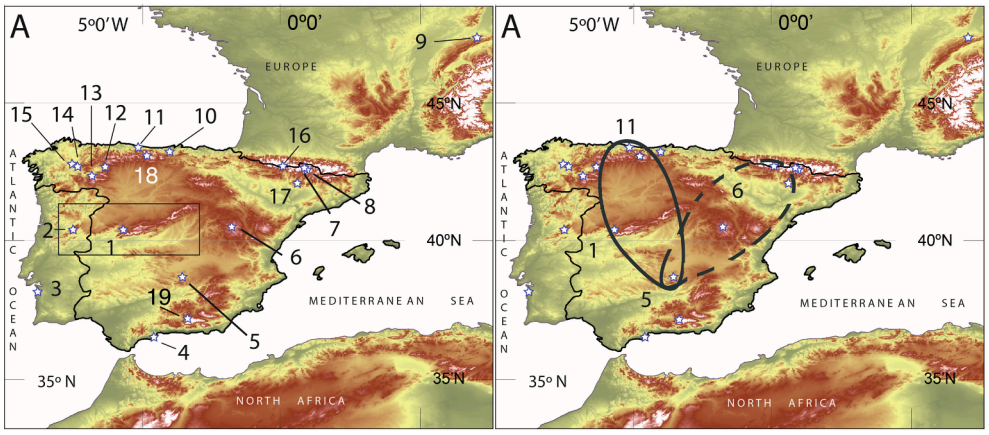

Fig. 7. (A) Black square, the ICS range. Sites of reference. 1: Navamuño. 2: Serra da Estrela (van der Knaap and van Leeuwen, 1997). 3: Lagoa de Traversa (Mateus, 1992). 4: El Refugio (Walczak, et al., 2015). 5: Columba volcano (Poblete-Piedrabuena et al., 2020). 6: Villarquemado (González-Sampériz et al. 2020). 7: Estany Redon (Camarero and Catalan, 2012). 8: Bassa Nera (Garcés-Pastor et al., 2017). 9: Lake La Gruère (Le Roux et al., 2012). 10: La Molina (Pérez-Obiol et al., 2016). 11: Roñanzas (Gallego et al, 2013), 12: La Mata (Jalut et al., 2010), 13: Sanabria. Muñoz-Sobrino et al.,(2004), 14: Cova Arcoia (Railsback et al., 2011), 15: Lucenza (Santos-Fidalgo et al., 2000), 16: Marboré (Oliva-Urcía et al., 2018), 17: Estanya (Morellón et al., 2009). 18: Lake Enol (Moreno et al., 2011). 19: Laguna Hondera (Mesa-Fernández et al., 2018). (B) Possible ashes plumes from the Columba volcano (5) and identified areas of probable influence: 1: Navamuño. . 6: Villarquemado. 11: Roñanzas.

Mn, Ca, Nb, Cr, Ti, and S show moderate or low positive loadings (<0.3); Zn, V, Zr, Cu, Pb, Fe, and Ni has low negative loadings; and P, Co, and Br show moderately negative loadings. Only Cl, associated with the Atlantic or anthropogenic sources, shows a high negative loading in this compartment. The high positive loadings of some lithogenic elements (K and Si) probably represent a detrital pool associated with a sedimentary imbalance (Haliuc et al., 2017). PC3 explains 8.9 % of the variance and is positively related to Mn and Si (with high loadings), Ni and Zn (moderate loadings), and Cr, Br, K, Al, Cu, Fe, and Co (low loadings), with Mn and Si showing the highest positive loadings. Thus, the positive direction of this PC3 component can probably be associated with coarser silt and sand-size fractions (Silva-Sánchez et al., 2016; Haliuc et al., 2017). Sr shows a very high negative loading (~-0.5), whereas Pb and Rb have moderately negative loadings. The elements that indicate variation in the organic matter (Ni, Zn, Br, and Cu) show moderate and low positive loads in PC3. The only firm positive peak over the entire Holocene in PC3 is at 5.8 ka cal BP (Fig. 6). However, because the redox behaviour of these elements may be related to their relative proportions, the content, nature of the secondary minerals, and changes in element mobility are associated only with redox conditions (Turu et al., 2018), which cannot be discarded below 14 m depth. Finally, PC4 captures 6.6 % of the total variance and is represented by very high positive loadings of Cl (at 2.8 ka cal BP; Figs. 3 and 6) and high negative loadings of Cu (i. e. at 5.8 ka cal BP; Figs. 3 and 6).

The counts per second (CPS) of the major and trace lithogenic elements (Al, K, Ca, Ti, Co, Fe, Si, Sr, Nb, Rb, and Zr) show a characteristic pattern of variation (Fig. 3), with moderate positive correlations observed between almost all of them (Table 3). Al has a moderately positive correlation with V, Mn, Fe, and Zn, while Si only shows a positive correlation with Al and a weak negative correlation with Br. A moderate positive correlation with Mn and a weak negative correlation with Br were observed for K. Ti has a high positive correlation with the majority of the aforecited lithogenic elements, but also a high positive correlation (0.78) with Fe and a moderately positive correlation with Cu, Zn, and Pb. Similarly, Co shows a high positive correlation with Ni, Cu, Zn, and Fe (0.81), whereas Zr has a moderately positive correlation with Fe, Ni, Cu, and Zn. Nb shows a moderate correlation with V, Fe, and Zn. Likewise, elements related to the organic matter content (P, S, Ni, Cu, Zn, and Br) also appeared to be positively correlated (Table 3). Cu and Zn show the highest positive correlations (0.78).In contrast, Fe, which, as mentioned above, shows a positive correlation with the other lithogenic elements (and a very high correlation with Ti and Co), also had a very high positive correlation (0.76) with Zn. Finally, Cl and Cr were weakly correlated with the other geochemical elements.

Table 3
Correlation coefficients (Spearman's rho) between the most representative XRF data. High positive correlations ($rs > 0.75$, $p < 0.001$) are marked in blue; moderate positive correlations ($rs = 0.51–0.75$, $p = 0.003$) in green; while weak negative correlations ($rs = -0.26$ to -0.50, $p = 0.05$) are in red.

	Al	Si	P	S	Cl	K	Ca	Ti	V	Cr	Mn	Fe	Co	Ni	Cu	Zn	Br	Rb	Sr	Zr	Nb	Pb
Al		0,56	0,36	0,24	-0,05	0,69	0,51	0,75	0,55	0,18	0,53	0,60	0,45	0,38	0,43	0,63	0,01	0,58	0,11	0,57	0,56	0,33
Si	0,56		-0,15	-0,12	-0,17	0,68	0,16	0,07	0,08	0,11	0,42	0,03	-0,03	-0,04	-0,12	0,14	-0,39	0,20	0,02	-0,05	0,06	-0,18
P	0,36	-0,15		0,36	-0,03	-0,05	0,40	0,52	0,39	0,00	0,13	0,42	0,41	0,38	0,49	0,42	0,53	0,22	0,08	0,46	0,36	0,47
S	0,24	-0,12	0,36		-0,11	-0,06	0,37	0,28	0,24	0,06	0,38	0,40	0,34	0,56	0,50	0,55	0,43	0,08	-0,22	0,41	0,27	0,15
Cl	-0,05	-0,17	-0,03	-0,11		-0,07	-0,21	0,03	0,02	0,03	-0,21	0,17	0,17	-0,09	-0,10	-0,17	0,19	-0,15	-0,09	-0,01	0,03	0,12
K	0,69	0,68	-0,05	-0,06	-0,07		0,32	0,40	0,25	0,15	0,53	0,35	0,16	0,08	0,00	0,29	-0,34	0,54	0,20	0,11	0,25	0,06
Ca	0,51	0,16	0,40	0,37	-0,21	0,32		0,57	0,34	0,02	0,45	0,38	0,26	0,30	0,32	0,52	0,19	0,50	0,51	0,53	0,44	0,27
Ti	0,75	0,07	0,52	0,28	0,03	0,40	0,57		0,65	0,16	0,45	0,78	0,62	0,46	0,57	0,69	0,27	0,61	0,14	0,74	0,71	0,51
V	0,55	0,08	0,39	0,24	0,02	0,25	0,34	0,65		0,06	0,32	0,53	0,48	0,35	0,40	0,49	0,21	0,40	0,03	0,50	0,51	0,33
Cr	0,18	0,11	0,08	0,06	0,03	0,15	0,02	0,16	0,06		0,13	0,21	0,19	0,15	0,12	0,16	0,05	0,06	-0,14	0,09	0,07	0,03
Mn	0,53	0,42	0,13	0,38	-0,21	0,53	0,45	0,45	0,32	0,13		0,55	0,38	0,36	0,36	0,64	0,05	0,43	-0,03	0,36	0,38	0,10
Fe	0,60	0,03	0,42	0,40	0,17	0,35	0,38	0,78	0,53	0,21	0,55		0,81	0,54	0,62	0,76	0,45	0,45	-0,15	0,64	0,58	0,49
Co	0,45	-0,02	0,41	0,34	0,17	0,16	0,26	0,62	0,48	0,19	0,38	0,81		0,51	0,58	0,65	0,50	0,33	-0,18	0,59	0,50	0,47
Ni	0,38	-0,04	0,38	0,56	-0,09	0,08	0,30	0,46	0,35	0,15	0,36	0,54	0,51		0,68	0,70	0,47	0,21	-0,25	0,55	0,39	0,33
Cu	0,43	-0,12	0,49	0,50	-0,10	0,00	0,32	0,57	0,40	0,12	0,36	0,62	0,58	0,68		0,78	0,54	0,35	-0,15	0,67	0,41	0,51
Zn	0,63	0,14	0,42	0,55	-0,17	0,29	0,52	0,69	0,49	0,16	0,64	0,76	0,65	0,70	0,78		0,41	0,54	-0,09	0,74	0,63	0,39
Br	0,01	-0,39	0,53	0,43	0,19	-0,34	0,19	0,27	0,21	0,05	0,05	0,45	0,50	0,47	0,54	0,41		-0,05	-0,20	0,41	0,23	0,47
Rb	0,58	0,20	0,22	0,08	-0,15	0,54	0,50	0,61	0,40	0,06	0,43	0,45	0,33	0,21	0,35	0,54	-0,05		0,44	0,50	0,55	0,35
Sr	0,11	0,02	0,08	-0,22	-0,09	0,20	0,51	0,14	0,03	-0,14	-0,03	-0,15	-0,18	-0,25	-0,15	-0,09	-0,20	0,44		0,09	0,12	0,24
Zr	0,57	-0,05	0,46	0,41	-0,01	0,11	0,53	0,74	0,50	0,09	0,36	0,64	0,59	0,55	0,67	0,74	0,41	0,50	0,09		0,64	0,50
Nb	0,56	0,06	0,36	0,27	0,03	0,25	0,44	0,71	0,51	0,07	0,38	0,58	0,50	0,39	0,41	0,63	0,23	0,55	0,12	0,64		0,38
Pb	0,33	-0,18	0,47	0,15	0,12	0,06	0,27	0,51	0,33	0,03	0,10	0,49	0,47	0,33	0,51	0,39	0,47	0,35	0,24	0,50	0,38	

The synthetic diagram in Fig. 6 is a plot of the Al/Ti and Mn/Fe ratios, LOI, MS, macro-charcoal abundance, four principal components derived from PCA, and the $\delta^{18}O$ record from the North Greenland Ice Core Project (NGRIP) (Rasmussen et al., 2014) plotted against the age model from Fig. 2. As approximated by the LOI, the total organic matter content in the core of Navamuño showed significant variability throughout the sequence (Fig. 6). LOI peaked 12 times (LOI 1 to 12; Fig. 6); however, the values were generally low, and its highest average content (>20 %) was observed in the upper 47 cm (23–30 %; 145 cal BP to the present) and in the sedimentary intervals: 146–107 cm (805–495 cal BP), 325–315 cm (28 %; 3.2–3.1 ka cal BP), 398 cm (4.7 ka cal BP), 454 cm (5.9 ka cal BP), 485 cm (maximum 36 % at 6.6 ka cal BP), 498–495 cm (6.9–6.8 ka cal BP), 705 cm (maximum 37 % at 10.6 ka cal BP), 779 cm (10.94 ka cal BP), 1340 cm (11.35 ka cal BP), 1421 cm (11.7 ka cal BP), and 1463–1458 cm (12.25–12.1 ka cal BP). The observed variability is due to the presence of layers that are rich in organic material (mainly plant debris), as described by Turu et al. (2018) and observed in the lithology of the core (Table 2).

Two highly positive MS peaks (>0.6 × 10ˆ3SI units) coincide with coarse sandy layers (Fig. 2) at 11.05 ka cal BP (839 cm) and 10.6 ka cal BP (705 cm), respectively, while the other peak occurs at ~11.37 ka cal BP (1350 cm) and is related to medium sands intermixed with dark brown silts (Fig. 6). Finally, a more recent moderate MS peak (>0.2 × 10ˆ3SI units) at 456 cm (5.9 ka cal BP) corresponds to dark brown sands. Noticeably, most of the PCA also peaked at 5.9 ka (Fig. 6).

Clay, silt, and peat coincide with relatively low MS values. For example, two minima in MS occurred at depths of 512–465 cm and 254–135 cm are related to peat accumulation.

The positively enriched sets of macro-charcoal particles are shown in Fig. 6; a stop abruptly at 11.4 ka cal BP and 10.7 ka cal BP. Such particles were practically absent between the Oldest Dryas and the Intra-Allerød Cold Period (IACP) (~15.6–12.9 ka cal BP), except for the upper part of the Bølling interstadial (~14.3–14.1 ka cal BP) and the lower part of the Older Dryas (~13.9–13.8 ka cal BP), when the accumulation of macro-charcoal reached 0.2–0.3 mm^2/g (Fig. 6). Rapid accumulation of macro-charcoal between the Allerød interstadial and the onset of the Holocene ~12.9–11.3 ka cal BP characterise this period, with peak values (1.6–2.2 mm^2/g) observed between 11.5 ka cal BP and 11.4 ka cal BP. Subsequently, two new maxima were recorded during the Early Holocene at ~10.9 ka cal BP (0.8 mm^2/g) and ~10.6 ka cal BP (2.96 mm^2/g). Macro-charcoals were still present with virtually continuous, relatively low values, from ~8.3 ka cal BP to 5.9 ka cal BP, disappearing and reaching a new peak (1.3 mm^2/g) at ~4.4 ka cal BP. Finally, the highest value (6.8 mm^2/g) of the whole sequence occurred during the Late Holocene at ~3 ka cal BP, although low values characterised this entire period.

6. Interpretation

Textural differences, rapid sedimentation, proxy peaking, and stratigraphic boundaries are all closely related. In addition, stratigraphical limits are overprinted onto the geochemical data (Fig. 3).

1) Between 16 ka cal BP and 12 ka cal BP, a surface boundary (SB; Fig. 3) separated the sediments with low organic matter content (LOI < 10 %; Fig. 4) from those with higher organic matter content (LOI > 15 %; Fig. 4). However, this period shows low geochemical sensitivity, except for S and P, which increased until 12 ka. During this period, the CH glacier receded and stabilised 3 km upwards from the ND (moraine ID-M3; Carrasco et al., 2015a). Its influence was negligible in the ND shortly thereafter since the glacier had receded until the upper valley (moraine ID-M4; Carrasco et al., 2015a).
2) A profusion of sedimentary changes is observed from 12 ka cal BP to 10 ka cal BP (Fig. 3), following the transition between the Early Holocene and the Upper Pleistocene. Changes such as diastems (unconformities, US) and base-level oscillations (maximum flooding surface, mfs; transgressive surface, TS) are observed on multiple stratigraphical surfaces (Turu et al., 2018). A basal surface of the forced regression (bsfr; Catuneanu, 2006; Turu et al., 2018) in the palaeolake may have been lowered its water level at this time, which is synchronous with the cold and probably arid period at ~11.4 ka correlating with the pre-boreal oscillation (PBO) (Björck et al., 1997). Kobashi et al. (2008) characterised this event (using ice-core δ15N measurements) as a gradual cooling over 100–150 years followed by abrupt warming of 4 ± 1.5 °C at 11.270 ka cal BP (Fig. 3).
3) Sets of the macro-charcoals increases before peaking at 8.0, 6.0, 4.5, and 3.0 ka cal BP (Fig. 6). P concentrations experienced rhythmic increases between 8.2 ka cal BP and 2.0 ka cal BP with pulses observed at 8.2–8.0, 8.0–7.3, 5.8–4.7, 4.7–4.0, 4.0–3.0, and 3.0–2.0 ka cal BP (the last of which was the final strong pulse) (Fig. 3).
4) Two hundred years of significant dust events occurred after the cold event at 8.2 ka cal B (Le Roux et al., 2012; Rodrigo-Gámiz et al., 2011), affecting Europe and North Africa. Le Roux et al. (2012) also indicated a change in the dust regime at 7 ka and 5 ka cal BP (from Sahara), which stabilised after 5 ka cal BP (Fig. 3) and changed at 2 ka cal BP.
5) The African Humid Period decline (Rodrigo-Gámiz et al., 2011) coincides with a high probability of an event at 7.3 ka cal BP surfaced, when V, Zr, Ti, Al, and Mn peaked (Fig. 3) and where lithogenic Hg, Zn, and Pb peaked in North Spain (Fig. 7 from Gallego et al., 2013). The moderate correlation between Ti and V (Table 3) should be related to fluctuations in the deposition of atmospheric dust (Rodrigo-Gámiz et al., 2011; Mesa-Fernández et al., 2018), both of which show a similar pattern throughout the recovered sequence (Fig. 3). The event probability at 7.3 ka cal BP also matches within a dusty period of unknown origin (7.4–7.2 ka cal BP; Le Roux et al., 2012), affecting Western Europe and led to a progressive reduction in the amount of tree pollen present in the region. The Al/Ti ratio increased during several periods (e.g. 12.8–11.1, 10.2, 9.4, 8.2, 7.3, and 6.6 ka cal BP), corresponding with incoming dust (Zielhofer et al., 2017b).
6) A sharp distinguishable peak at 5.8 ka cal BP indicates a Cu-rich layer (Fig. 3), too early for ore mining activities. However, Hg-rich sequences have already been identified in Roñanzas (Fig. 7a; Gallego et al., 2013). These authors associated this Hg peak with volcanic dust.
7) The probability of an event is high at 4.9 ka cal BP when PC2 shifts (Fig. 6). The high relative P values and S peaks (Fig. 3) suggest extra-basin influxes, which was probably in the form of dust from North Africa (Fitzgerald et al., 2015; Camarero, 2017), as it is the case for Sierra Nevada (Mesa-Fernández et al., 2018). Nowadays, a higher frequency of positive North Atlantic Oscillation (NAO) values in its half-period correlates with frequent dusty episodes, carrying P from Northern Africa to Iberia (Camarero and Catalan, 2012; Lake Redon, Fig. 7a). These authors demonstrated a good correlation between P deposition and the NAO index in mountain lakes from the high Pyrenees (Camarero, 2017). Vannière et al. (2011) invoked a NAO-like climate modulation during the Holocene in Western Europe, embracing the ND, and Rodrigo-Gámiz et al. (2011) report predominant positive NAO index when SD exportation intensifies.
8) A final Cl pulse is observed between 2.8 ka cal BP and 2.0 ka cal BP, characterised by its strength, while P shows an increase at 2.8 ka cal BP (Fig. 3). Batting behaviour was observed for Cl, that is, slightly upward decreasing pulses between 7.3 ka cal BP and 2.8 ka cal BP (Fig. 3). Oceans provide the largest source of atmospheric Cl to terrestrial ecosystems (Keppler et al., 2004); thus, once Cl is captured from organic matter, it can be found in deposits following precipitation or on the sedimentary bed when transport ceased.
9) The event probability is high at 1.2 ka cal BP (Fig. 3) and may be associated with Bond event 1; however, this event could also result from anthropogenic activities.

7. Discussion

7.1. Deglaciation: Oldest Dryas stadial (~15.6–14.7 ka cal BP)

The oldest dated sample from the bottom of the core at a depth of 1600 cm (Table 1; ~16.56 ka cal BP; Turu et al., 2018) corresponds to phases in which the CH palaeoglacier retreated (Carrasco et al., 2013, 2015a), and the sediments deposited between 1600 cm and 1562 cm are synchronous with the onset of the Oldest Dryas (Greenland Stadial 2a/GS-2a). A maximum flooding surface (msf, Fig. 3; Turu et al., 2018) reveals the transition between the moist to dry bi-phase hydroclimate reorganisation after the iceberg discharges of Heinrich Event 1 and to characterise the Oldest Dryas (Pérez-Mejías et al., 2021). The so-called Mystery Interval (Denton et al., 2005; 2006; Williams et al., 2012) was initially identified in other Iberian ranges ~16.56–14.7 ka cal BP (Jalut et al., 2010; Domínguez-Villar et al., 2013; Palacios et al., 2016). This period has also been recorded in marine pollen sequences around the Iberian Peninsula as a cold and dry interval (Naughton et al., 2007, 2019; Fletcher et al., 2010. The ND shows the lowest sedimentation rate (0.23 mm/yr) in the Oldest Dryas (Fig. 2). These data are consistent with the low MS values (Fig. 6) and fine-grained deposits (greenish to greyish clay and clayey silt; Fig. 2; Table 2) observed in the ND. The non-laminated clays at the bottom of the core originated from a glaciolacustrine environment in an amictic lake (Turu et al., 2018), similarly to those described in other glacial lakes of the Pyrenees and the Cantabrian Mountains (González-Sampériz et al., 2006; Jalut et al., 2010; Oliva-Urcía et al., 2018; Turu et al., 2018), and Serra da Estrela (van der Knaap and van Leeuwen, 1997). Analyses of northern Iberian inland lakes also show a similar climate pattern; with the Oldest Dryas corresponding to an arid and cold period (Morellón et al., 2009; González-Sampériz et al., 2010; Ruiz-Fernández et al., 2016); however, the ND reveals that the climate was more complex during this stadial.

PC1 (positive side; Fig. 5) reflects the changes between an allochthonous to autochthonous sedimentation supply (Fig. 6), likewise a high Al/Ti ratio (Höbig et al., 2012; Schröder et al., 2018) and the latter by various indicators as low MS values or low amounts of Al, Ti, K, Ca, Co, Nb, Si, Fe, Rb, and Zr (see Figs. 3, 4, and 6). Therefore, the relatively high water levels and the abundance of lithogenic elements such as Fe or Ti at the Oldest Dryas coincided with an intense soil erosion during deglaciation, with low Mn/Fe ratios (Martín-Puertas et al., 2011). Series of lithogenic elements, including Ti, K, Rb, and Zr, are commonly considered indicators of watershed erosion (Koinig et al., 2003). The high correlation (0.68) between K and Si (Table 3) in the ND suggests that Si mainly comes from K-Aluminosolicates, also related to PC2 (Figs. 4 and 5) (Haliuc et al., 2017), with relatively high values during the Oldest Dryas (Fig. 6).

These studies infer that a sharp decrease in the mean annual air temperature reducing the yearly precipitation to half of its current value. In addition, the lower organic productivity in the palaeolake (LOI content, Fig. 6) is attributed to the cold conditions in the Pyrenees during this period (González-Sampériz et al., 2006; Pèlachs et al., 2011).

7.2. A complex Bølling/Allerød interstadial (~14.7–12.6 ka cal BP)

7.2.1. Sedimentary record

The ND base level remains relatively shallow and stable during this period and prevails until 12.6 ka cal BP. Hydromorphic soils are described by Turu et al. (2018), indicating dominant dark-grey-brown clayey silt and dark green–brown silty clay between 1562 cm and 1485 cm (Fig. 2; Table 2). There is a significant decrease in PC1 values and lithogenic elements (e.g. Al, K, and Zr), parallel to the PC3 increase (S, P, Ni, and Zn), between 1562 cm and 1542 cm, as a result of an increase in the water table level (Turu et al., 2018) during the Bølling sub-interstadial period (Greenland Interstadial GI-1e; ~14.7–14 ka cal BP) (Figs. 3 and 6). At that time, the NGRIP Greenland core (Fig. 6) shows an abrupt increase in the $\delta^{18}O$ values (Rasmussen et al., 2014), indicating global wetter and warmer conditions. An increase in organic productivity is accompanied by an LOI (>10 %) rise and a temperature increase (Fig. 6) in parallel to rainfall (López-Sáez et al. 2020). The pollen data indicates that the Béjar area was a refuge for temperate vegetation during the Bølling oscillation (López-Sáez et al., 2020).

At the onset of the Older Dryas sub-interstadial (Fig. 2; Table 2), the Bølling lacustrine dark-grey-brown clayey silts transitioned, under permanent flooding (Turu et al., 2018), into dark green silty clay and low Mn/Fe values (Fig. 6). Chromogenic responses (Naeher et al., 2013) indicates low redox conditions (Turu et al., 2018) resulting from water level fluctuations, mineral inputs (clays and oxides) and poorly oxygenated waters (Davison, 1993) in the lake. Discolouration and leaching occur in a changing redox environment when chromogenic compounds, like Mn and Fe, vary their oxidation state at low redox potential (Davison, 1993; Koinig et al., 2003; Haliuc et al., 2017).

During the Older Dryas (14.0–13.4 cal yr BP; GI-1d; 1543–1520 cm depth), high values of Zn (Fig. 3) may indicate anoxic conditions in the ND since this element is considered a palaeo-redox indicator (Dean et al., 1997). Zn also shows a high positive (0.76) correlation with Fe and a moderate correlation (0.64) with Mn (Table 3). The atmospheric conditions are attributed to a negative NAO-like index during this period (Rodrigo-Gámiz et al., 2011) and weak westerlies over the Gulf of Lion, a somewhat unmatching pattern for SD migration northwards.

During the Greenland Interstadial GI-1c (~13.4–13.1 ka cal BP; 1520–1515 cm), the geochemical trend shows an increase of Al/Ti ratio, PC1 and PC2 and ends in a sharp rising end, also observed in the $\delta^{18}O$ values of the NGRIP Greenland core (Fig. 6; Rasmussen et al., 2014), similarly at the Allerød oscillation (Greenland Interstadial GI-1a; ~12.9–12.6 ka cal BP; 1500–1485 cm). The Allerød in the ND, the Mn/Fe ratio (0.2) increase (Fig. 6), indicating more oxygenated waters (Haliuc et al., 2017; Oliva-Urcía et al., 2018) in the ND.

The complexity of the processes presented in our study, which include the first phase of glacial retreat during the Oldest Dryas and a later stage of glacial re-advancement during the arid and cold Older Dryas in northern Iberia, have rarely been documented (González-Sampériz et al., 2006; Morellón et al., 2009; Jalut et al., 2010; Aranbarri et al., 2014; Moreno et al., 2014; Palacios et al., 2016; Camuera et al., 2018, 2019).

7.2.2. Macro-charcoal particles

Macro-charcoal particles were present only in the upper part of the Bølling sub-interstadial at ~14.3 ka cal BP (0.2 mm^2/g, Fig. 6). These results indicate a low fire activity in the ND; thus, shortage of biomass to sustain fire (López-Sáez et al., 2020), and It may have resulted from the cool summers and low winter temperatures (Pèlachs et al., 2011).

The sedimentation rate also increased (0.33–0.52 mm/yr; Fig. 2), probably related to an enhanced erosion of nearby slopes due to a higher frequency of palaeofires. The Al/Ti ratio reduction also advocates for allochthonous sedimentation in the ND (Fig. 6) in GI-1d, specifically in its middle part. The MS also increases around ~13.8 ka cal BP. The fire activity in the ND is evidenced by a small macro-charcoals production (0.3 mm^2/g) at ~13.8 ka cal BP (Fig. 6). Through stadials or cold sub-interstadial periods (Daniau et al., 2007), the scarcely available fuel may have resulted in the low fire activity around the ND during the Older Dryas sub-interstadial. However, charred particles are abundant in Serra da Estrela during GI-1d (Connor et al., 2012). Biomass burning differences whithin the western ICS suggests a westward modulation from the climate regime between ND and Serra da Estrela. Nevertheless, in South Iberia macro-charcoals also peak (Carrión, 2002) at GI-1d.

The summer temperature increased progressively at the Allerød warm interval (López-Sáez et al., 2020) alongside the fire frequency. Macro-charcoal particles values doubled from 0.12 mm^2/g to 0.44 mm^2/g (Fig. 6) during the Allerød oscillation ~12.9 –12.6 ka cal BP, and a similar pattern is for Serra da Estrela (Connor et al. 2012). The abundance of macro-charcoal, the high values of PC1 and the increasing sedimentation rate (0.23–0.91 mm/yr) during the warmer and wetter

Bølling and Allerød periods are related to the input of fine grain-sized sediment that resulted from enhanced erosion on fragile soils (Figs. 2 and 6). When warm interstadial episodes and high Al/Ti ratio match (Fig. 6), the ND is feeded in terrigenous influx from runoff (Höbig et al., 2012; Schröder et al., 2018). This interpretation is consistent with other Iberian palaeoenvironmental records that show a similar warming behaviour and humidity increase during the Bølling, GI-1c and Allerød periods (González-Sampériz et al., 2010; Aranbarri et al., 2014; García-Alix et al., 2014; Iriarte-Chiapusso et al., 2016; Tarroso et al., 2016; Camuera et al., 2018, 2019).

7.2.3. Palaeoenvironmental inferences

The Bølling/Allerød interstadial period (Greenland interstadial GI-1) has been widely recorded in most inner Iberian sequences, especially in high-mountain environments, and is characterised by warmer summer temperatures and higher glacier meltwater pulses (Morellón et al., 2009; Carrión et al., 2010; Jalut et al., 2010; González-Sampériz et al., 2010; Moreno et al., 2014; Camuera et al., 2018). The only known evidence of this interstadial in the ICS comes from the palynological records of the Charco da Candieira Lake in Serra da Estrela (van der Knaap and van Leeuwen, 1997) (Fig. 1) and the corresponding core from Navamuño (Turu et al., 2018; López-Sáez et al., 2020). Rapid cold oscillations from 14 ka cal BP to 13.4 ka cal BP separate the GI-1e (Bølling sub-interstadial) from the GI-1c warm episodes (GI-1d; Rasmussen et al., 2008, 2014). The Older Dryas (GI-1d) may be present as a sharp decrease in allochthonous elements, such as Al, Ti, K, Ca, Co, Rb, Si, Sr, Fe, Zr (Fig. 3), the PC1 values (Fig. 6), and by an abrupt decrease in the $\delta^{18}O$ values (Rasmussen et al., 2014). Similar conditions have been found by in the northern and southern Iberian territories, mainly in mountain environments, including the westernmost ICS (van der Knaap and van Leeuwen, 1997). During this period (GI-1d), low LOI production is observed, with variable Mn, Ni, and S (Fig. 3) values and a notable reduction in the PC2 and PC4 values (Figs. 3 and 6). These data indicate a significant decrease in the contribution of terrigenous sediments and detrital input, including a substantial reduction in the organic matter production within the palaeolake. When comparing episodes, an increase in the PC2 values occurred during the three warm periods (Fig. 6), with the latter two were related to fluxes of sediment reaching the ND (GI-1c and Allerød). The Bølling sub-interstadial was cooler than the Allerød interstadial, as indicated by the weaker development of organic matter (LOI, Fig. 6). The latter suggests a warming trend from the Bølling to the Allerød, which is archived in both the marine and the terrestrial records in the southwestern Mediterranean region and southern Europe (Watts et al., 1996; van der Knaap and van Leeuwen, 1997; Renssen et al., 2010; Yu and Eicher, 2001; Naughton et al., 2007, 2019; Morellón et al., 2009; Carrión et al., 2010; González-Sampériz et al., 2006, 2010; Jalut et al., 2010; Rodrigo-Gámiz et al., 2011; Moreno et al., 2014; de Beaulieu et al., 2017; Sadori, 2018). However, a second cold and dry period were detected later in the Bølling/Allerød interstadial at ~13.1–12.9 ka cal BP (1515–1500 cm), and it may correspond to the so-called IACP (Greenland Interstadial GI-1b, Fig. 6), and resulted in a decrease in the $\delta^{18}O$ values (Rasmussen et al., 2014). Lithogenic elements (Al, Ti, Si, Fe; Fig. 3) decrease in the Older Dryas while increase during GI-1c; however, the low resolution of this portion of the core makes the interpretation difficult. The PC1 and PC2 values decreased alongside the LOI, while the Al/Ti ratio increased during the IACP (Figs. 3 and 6). A similar smaller decrease in the Mn/Fe ratio in the IACP period is likely to have occurred during the Older Dryas, although smaller, suggesting poorly oxygenated water (Davison, 1993; Haliuc et al., 2017). Palaeoclimate similarities are prominent for GI-1d and IACP in the study area, experiencing dry and cold phases.

7.2.4. Extra-basin gain

A geochemical overprint in the sedimentary records of the ND coincides with a strong negative peak for PC4 (Fig. 6), MS increases (Fig. 6) and peaks from Rb and Zn are at ~13.7 ka cal BP; and this could be the effect of the Columba volcano (Fig. 7a) over the ND, in which erupted around 13.845 ± 0.268 ka cal BP (Poblete-Piedrabuena et al., 2019). Nevertheless, inputs from remote source areas such as volcanic ash or dust from Asian deserts dust (Grousset and Biscaye, 2005) overprint the local sediments in Western Europe at 12.8 ka cal BP (Le Roux et al., 2012). The positive trends of P, S, and Ca simultaneously reduced the Al, K, and Cl contents in the sediments (Fig. 3), driving a change in the trend of PC1, PC2, and PC4 at 12.8 ka cal BP (Fig. 4). Additionally, the inferred temperatures and precipitation that the ND pollen data concludes (López-Sáez et al., 2020) were at 12.8 ka cal BP in a maximum. Liquid droplets formed from dust particles acting as nuclei within clouds (Fitzgerald et al., 2015), favouring precipitation and heat transport. Tree pollen percentages increased in the ND (López-Sáez et al., 2020) during 12.9–12.6 ka cal BP, suggesting warm and wet (oceanic) conditions in the westernmost ICS (van der Knaap and van Leeuwen, 1997).

7.3. Climatic variability within the Younger Dryas stadial (~12.6–11.7 ka cal BP)

The Greenland Stadial 1 (GS-1) abrupt event, usually referred as to the cold and dry YD, occurred at the end of the Late Glacial warming and just before the onset of the Holocene (Alley, 2000; García-Ruiz et al., 2016; Tomasso et al., 2018). According to the age-depth model of the Navamuño record (Fig. 2) and the multi-proxy analyses between 1485 cm and 1420 cm, the YD period is considered to have occurred between ~12.6 ka cal BP and 11.7 ka cal BP (Figs. 3 and 6). The YD has been recorded throughout the Mediterranean and southern Europe by several proxies in both continental and marine sites (Muñoz-Sobrino et al., 2013; Morellón et al., 2009; Carrión et al., 2010; Fletcher et al., 2010; González-Sampériz et al., 2010; Jalut et al., 2010; Moreno et al., 2011, López-Merino et al., 2012; Aranbarri et al., 2014; Baldini et al., 2015; Bartolomé et al., 2015; García-Ruiz et al., 2016; Iriarte-Chiapusso et al., 2016; Camuera et al., 2018; Tomasso et al., 2018; Naughton et al., 2019; López-Sáez et al., 2020). The YD is documented in Greenland ice cores (Fig. 6) by low and oscillating $\delta^{18}O$ values (Alley, 2000; Rasmussen et al., 2014).

The YD is characterised by a drop of the water level in the ND, as indicated by the deposition of dark brown silty clay (Fig. 2; Table 2), along with a sharp decrease in the Al/Ti ratio (Fig. 6). During the Early YD (~12.6–12 ka cal BP), the Mn/Fe ratio increased (Fig. 6), pointing to fresh oxygenated water in the ND (Haliuc et al., 2017). The presence of organic matter renders sediment the dark brown colour characteristic of marshy related deposits (Turu et al., 2018). This Early YD phase is characterised by increasing values of P and S, as well as high values of Zr, Ni, and Mn. Br values appear for the first time in this sequence. However, Notably, P, Br, S, and Ni are related to organic matter (Koinig et al., 2003; Kylander et al., 2011). Furthermore, the presence of Br pertains to the processes controlling the enzymatic halogenation of organic matter (Van Pee and Unversuch, 2003; Leri and Myneni, 2012) or biomass burning (Dai and Chiao, 2019). The continuous presence of macro-charcoals, with a peak (1.3 mm^2/g) at ~11.9 ka cal BP, along with an increase in the sedimentation rate (0.85–1.18 mm/yr) and high values of both PC1 and PC2 ~ 12.6–12 ka cal BP (Fig. 6), that are related to terrigenous sediment input, indicate enhanced soil erosion. The main lithogenic elements involved in this phase are Ca, Zr, Ti, and Sr, while Al, K, Rb, and Si generally decreased throughout the YD (Fig. 3).

A phase of low fuel availability is mainly related to steppe-type vegetation (Connor et al., 2012). This match in the ND only for the beginning of the YD, that is: sustained organic matter content since the Allerød culminating in two LOI peaks (numbers 12 and 11) at ~12.25–12.1 and 11.7 ka cal BP (respectively) with subsequent increases of charred material (macro-charcoals; Fig. 6). Like the Portuguese ICS record (Connor et al., 2012), high macro-charcoal values in the ND may refer to local fires mediated by the aridity (Daniau et al., 2007; López-Sáez et al., 2018a, 2018b) at the end of the Younger Dryas. Posteriorly, charred particles increase in Serra da Estrela at ~12–11 ka

cal BP (Connor et al., 2012), between the end of the Younger Dryas (YD) and the beginning of the Holocene.

Surface enrichment with Mn with Fe is probably related to the vadose oxic conditions during the period ~12.6–12 ka cal BP, which provided favourable conditions for forming oxidised and immobile forms of the elements (Chesworth et al., 2006). The decreasing values of both PC1 (which reflects the relative input of lithogenic versus organic sediment) and PC2 (interpreted as from detrital gain) during the Late YD (~12–11.7 ka cal BP) (Fig. 6) indicate possible conditions of desiccation, subaerial exposure and the establishment of marsh-type vegetation. Both principal components point to a relatively deep wetland within stable wet and cooler climatic conditions during the second half of the YD. Higher PC3 values and a lower Mn/Fe ratio (Fig. 6) also represent the possibility of significant water saturation of sediments that formed in less-oxygenated water (Davison, 1993).

In summary, our results suggest higher saturation of the sediments, probably from groundwater (Carrasco et al., 2018) during the first phase of the YD (~12.6–12 ka cal BP) may reflect enhanced precipitation, whereas the following second phase (~12–11.7 ka cal BP) which may be due to a more efficient hydrological cycle (López-Sáez et al., 2020); however, negatively balanced.

A transitional biphasic structure is for the YD. A similar palaeoclimate pattern to that in the ND was also been documented by van der Knaap and van Leeuwen (1997) in their study on Serra de Estrella, by Aranbarri et al. (2014) and by Wei et al. (2019) in their study on the Villarquemado palaeolake (Fig. 1), or at several northern Iberian sites (Moreno et al., 2011; Muñoz-Sobrino et al., 2013; Baldini et al., 2015; Bartolomé et al., 2015; Iriarte-Chiapusso et al., 2016; García-Ruiz et al., 2016). For example, the Sanabria lake record (Fig. 7a) includes an initial cool and wet phase (~12.9–12.4 ka cal BP) followed by a subsequent warm and dry phase (12.4–11.7 ka cal BP) (Muñoz-Sobrino et al., 2004). Morellón et al. (2018) pointed out a similar climate structure within the YD, perhaps due to a latitudinal-like drifting of palaeoclimatic and palaeohydrological conditions affecting the Iberia Peninsula as observed by Naughton et al. (2007).

7.4. The Pre-Boreal and the Early Holocene (~11.7–10.2 ka cal BP)

7.4.1. Sedimentary record

Three MS peaks (numbers 4 to 2) at ~11.37, 11.05, and 10.6 ka cal BP (Fig. 6), are associated with a dramatic increase in the particle size. These are related to a quasi-single event associated with basin instability and subsidence (Carrasco et al., 2018; Turu et al., 2018). The increase in the sedimentation rate from 1330 cm to 785 cm during the Late Pre-boreal (~11.3–10.95 ka cal BP), which reached average values of 14.89 mm/yr and peaked at 100 mm/yr to 11.12 ka cal BP (Fig. 2), clearly marks a sudden change in the sedimentary regime (Turu et al., 2018), probably tectonically induced. However, multiple factors may have interacted to affect the stability of the ND at 11.4 ka cal BP when dark brown silts were deposited over coarse sand at ~11.05 ka cal BP (Fig. 2; Table 2), and coinciding with an MS peak (number 3; Fig. 6) correlated with Fe (Fig. 3). Rapid changes in the environmental magnetic behaviour of the sediments occurred during this period and the main MS facies. Therefore, the MS fluctuation likely correlates with the changes in the composition of the allochthonous and lithogenic sediment components, all of which show high values (Fig. 3), overprinted by syn- and post-sedimentary redox changes, as suggested by the Mn/Fe ratio at ~10.9 ka cal BP (Fig. 6) and the Mn peak (Fig. 3). K, Si, and Sr, indicative of detrital input into the basin (Kylander et al., 2011), show a strong correlation with the high positive values of PC2 (Figs. 4 and 5) in this part of the sequence at ~11.3–10.95 ka cal BP. Still, these values declined or fluctuated until the end of the Early Holocene (Fig. 3).

Three concomitant peaks in the Al/Ti and Mn/Fe ratios were observed at ~10.9 ka, 10.2 ka, and 9.8 ka cal BP (Fig. 6), indicating a sedimentary environment with relatively well-oxygenated waters (Davison, 1993; Schröder et al., 2018). Therefore, geochemical data (Cl) pointed to an oceanic influence (Fig. 3) in two of these three periods during the Early Holocene in (11–10.9 ka cal BP and 10.2–10.0 ka cal BP).

7.4.2. Loss-on-ignition and macro-charcoal particles

López-Sáez et al. (2020) explained an increase in rainfall and temperature with three high LOI peaks at ~11.35, 10.94, and 10.6 ka cal BP in the ND (numbers 10 to 8; Fig. 6) and belongs to the beginning of the Holocene. The peaks coincide with a rapid and constant accumulation of macro-charcoal at ~11.5–11.3, 10.9–10.8, and 10.6 ka cal BP. Biomass burning resulted in significant macro-charcoal concentrations in the ND (Figs. 3 and 6). The cumulative fire activity, evidenced by the charcoal-increase in the ND starting at ~11.7 ka cal BP, arrives at its climax around ~11.30 ka cal BP, as in Serra da Estrela (Connor et al., 2012). In parallel, we found a peak in LOI (11.35 ka cal BP; number 10) and the corresponding rise in MS (11.37 ka cal BP; number 4) when a high concentration of charred particles occurs (Fig. 6).

A new charcoal increase in the ND starts after the Pre-Boreal oscillation (PBO) event (~11.4 ka cal BP) and arrives at its maximum at ~10.70 ka cal BP (Fig. 6). Moreover, a new bromine peak at ~10.6 ka cal BP appears to be related to the high LOI percentages or high organic matter content (Van Pee and Unversuch, 2003; Leri and Myneni, 2012) that result from the burning of biomass (Dai and Chiao, 2019). Conversely, in Serra da Estrela, fire activity is found at its minimum (Connor et al., 2012). Biomass burning differences within the western ICS suggests an eastward modulation from the climate regime between Serra da Estrela and the ND. In south Iberia, a single cumulative pulse of charred particles began at ~11.5 ka cal BP and culminate at ~10.2 ka cal BP (Carrión, 2002).

Palaeoburning could have eliminated vegetation that protected soils in the catchment area from the ND, resulting in increased erosion. Notably, the Ericaceae peak and the presence of *Plantago*, *Artemisia*, *Aster*-type, and Chenopodiaceae (López-Sáez et al., 2020) suggest environmental disturbances at 10.6 ka cal BP.

7.4.3. Palaeoenvironmental inferences

During the first interval of the Early Holocene at ~11.7–11.45 ka cal BP, the core record (1420–1375 cm) shows a transition from dark green silty clay to a mixture of sands and silts of different colour tonalities, with a consistently increasing sedimentary rate (1.18–1.47 mm/yr) (Fig. 2; Table 2). The Al/Ti and the Mn/Fe ratios decreased, coinciding with the LOI, PC1, PC2, and PC4 values, while the MS and PC3 values progressively increased (Fig. 6). These trends could indicate a new base-level rising after the YD, with moister organic soils comprising coarse silts and sand-size fractions from reduced detrital input (Kylander et al., 2011). A shallow lagoon or, more likely, a floodplain is interpreted to exist in the ND at this period because palaeosols' appearance does not favour a permanent lake's existence (Carrasco et al., 2018). According to the age-depth model (Fig. 2), the timing of the marked changes belongs to the Early Pre-boreal, when a rapid temperature rises and prevails in many European palaeoenvironmental records (Björck et al., 1997; Fisher et al., 2002; Peyron et al., 2005; Bos et al., 2007), along with the abrupt increase in the $\delta^{18}O$ values (Fig. 6) observed in the NGRIP Greenland core (Rasmussen et al., 2014). Additionally, most lithogenic elements and PC1 values decreased (Figs. 3 and 6), except for Si and Zr, which increased (Fig. 3). Zr is commonly associated with silt and coarser fractions; its high value, therefore, indicates the deposition of coarser grains and may be used as a proxy of the energy of the sedimentary process and grain size (Kylander et al., 2011). Moreover, the increase of Si is consistent with high base levels (Morellón et al., 2009). The decrease in LOI is also compatible with the lower values of most biophilic elements (Figs. 3 and 6). The increasing trend in the MS measurements probably reflects fire activity in the ND, which is also evident from the substantial increase in macro-charcoals (Fig. 6), related to wetter conditions and runoff (Mesa-Fernández et al., 2018).

In the ND, this event was evident in relatively high water levels (TS,

Fig. 3) that coincided with all the principal components (Fig. 6). These data concur with the increase in most lithogenic (Al, Ti, K, Ca, Co, Rb, V, Cr, and Fe) and biophilic (S, Cu, and Zn) elements, except for Si and Zr (Fig. 3). This climate anomaly has been evidenced by numerous pollen records throughout Iberia (González-Sampériz et al., 2010; Burjachs et al., 2016; Iriarte-Chiapusso et al., 2016), including the western ICS (van der Knaap and van Leeuwen, 1997; López-Sáez et al., 2020). The following trends suggest a base-level drop and dominant ephemeral water conditions, increasing the number of lithogenic elements (especially of medium sands) and detrital input (Fig. 2; Table 2). These resulted from the erosive processes associated with a decrease in the base level (US boundary at 11.1 ka cal BP; Fig. 3) and the subsequent recurrence of local fires (Koinig et al., 2003; Haliuc et al., 2017).

LOI values generally declined except for a peak (number 9) at ~10.94 ka cal BP, which is synchronous with significant macro-charcoal concentrations (0.81 mm^2/g) and some biophilic elements such as P, S, Ni, and Zn (Figs. 3 and 6). Low MS values indicate high organic matter content (LOI peak at 10.94 ka cal BP, number 9; Fig. 6). Comparison of the MS, LOI and XRF records (Figs. 3 and 6) suggests that the section between 1330 cm and 785 cm (Fig. 2) most likely corresponds to a change in the geomorphological configuration of the study area. Hydromorphic soils, typical of a marshy environment, predominated during the YD and gave way to an alluvial system during this phase of the Early Holocene (Turu et al., 2018; López-Sáez et al., 2020). According to the geophysical studies carried out by Carrasco et al. (2015b, 2018), lateral accretion with a meander-type pattern infilled a portion of the ND. Subsequently, the sedimentation rate seemed to decrease from 2.19 mm/yr (until 10.68 ka cal BP; 700 cm) to 0.53 mm/yr (until 8.2 ka cal BP) (Fig. 2), followed by a stepwise decrease in the MS and further gradual increase in the values that culminated in a peak at ~10.6 ka cal BP (number 2) at a depth of 705 cm, with accordingly high values of both LOI (number 8) and macro-charcoals (Fig. 6). Jalut et al. (2000) described posterior Pre-boreal arid phases around 10.9–9.7 ka cal BP, resulting in climatic variation in Western Iberia. *Pinus* was not predominant during the Early Holocene (Serra da Estrela; van der Knaap and van Leeuwen, 1995); however, a xerothermic-to-mesothermic oak-forest succession resulted from a wetter climate 8 000 years ago in the ICS (Pérez-Obiol et al., 2011).

7.4.4. Extra-basin gain

The relative Cu peak at 11.4 ka cal BP (Fig. 3) suggests the influx of ash, probably from the Calatrava volcanic field (Fig. 7a), which was still active (Poblete-Piedrabuena et al., 2019) at the time.

The highest values of Cl at ~10.9–10.8 ka somewhat recurrent at 10.2 ka cal BP, the Ca and K peaking and reduction in P and S (Fig. 3) suggest brief oceanic spells from the Atlantic embracing the western ICS.

7.5. The Early Holocene (~9.8–8.2 ka cal BP)

In general, the XRF data shows that both lithogenic and biophilic elements remained relatively stable between ~9.8 ka cal BP and 8.2 ka cal BP (Fig. 3). However, two noteworthy events occurred during this time. The first one was related to an abrupt climatic event at ~9.3 ka cal BP, following which the Al/Ti and Mn/Fe ratios and the PC1-PC3 values decreased until 8.2 ka cal BP, while the MS slightly increased (Fig. 6). These data coincide with a decrease in all the lithogenic and biophilic elements (Fig. 3), suggesting a phase with frequent low-oxygenated waters (Davison, 1993). Floodplain replaced the alluvial plain that occupied the ND over much of the Pre-Boreal, explaining the abundance of silts (Fig. 2; Table 2). The increase in magnitude, frequency of rainfall and surface runoff (low Al/Ti ratio) can be interpreted as flooding in the ND (Koinig et al., 2003; Kylander et al., 2011). This abrupt climate event at ~9.3 ka cal BP, which corresponds to one of the isotopic anomalies registered in the Greenland ice cores (Rasmussen et al., 2014; Fig. 6), has also been documented in the Iberian records. It was a cold and wet period in the northern Peninsula (González-Sampériz et al., 2006; Morellón et al., 2009; Iriarte-Chiapusso et al., 2016; Pontevedra-Pombal et al., 2019) and a dry period in south Iberia (Jalut et al., 2000; Carrión, 2002; Naughton et al., 2007, 2019; Carrión et al., 2010; Mesa-Fernández et al., 2018) suggesting a latitudinal-like boundary of palaeoclimatic and palaeohydrological conditions around 40° N.

The second notable period corresponds to ~8.2 ka cal BP (Alley et al., 1997), and is widely documented in the Iberian Peninsula through numerous proxies as an arid and cold interval (López-Sáez et al., 2008; Morellón et al., 2009; Carrión et al., 2010; Pontevedra-Pombal et al., 2019). This period is also indicated in the NGRIP Greenland core (Fig. 6) by a decrease in $\delta^{18}O$ values (Rasmussen et al., 2014). The only reference to this abrupt event in the ICS comes from several pollen records at its westernmost extreme (van der Knaap and van Leeuwen, 1995; López-Sáez et al., 2014, 2017).

A maximum flooding surface (msf, Fig. 3) reveals the transition between the 9.3 and 8.2 ka cal BP cold periods; however, flooding was presumably low as the Mn/Fe ratio increased (Davison, 1993). PC1 and PC2 were sharply positive at 9.0 ka cal BP (Fig. 6) using P to compute the rise in palaeotemperature (Fig. 3). The PC1 only remained positively while the PC2 was negative at 8.4 ka cal BP (Fig. 6), probably related to a pronounced dusty and arid period before 8.2 ka cal BP (Le Roux et al., 2012). A positive peak in Al/Ti (Fig. 6) and the calculated drop in the palaeotemperature (Fig. 3) evidence a cold event at 8.2 ka cal BP. A peak in the charcoal concentration was observed in the record of Maíllo (Fig. 1) at ~8.1–8.0 ka cal BP (Morales-Molino et al., 2013), as well as the ND (Fig. 6). These charcoal particles are related to increased fire activity at ~8.2 ka cal BP, probably linked to dry climatic conditions (Vannière et al., 2011).

7.6. Beginning of the Mid-Holocene (~8.2–5.9 ka cal BP)

7.6.1. Palaeoenvironmental inferences

García-Álvarez et al. (2017) reported that the ancient *Pinus gr. sylvestris* forests in Sierra de Gredos included many deciduous *Quercus* during the Early and Mid-Holocene, especially between 1900 and 2000 m (a.s.l). This period (~8.2–7.6 ka cal BP at 558–531 cm depth; Fig. 2) is characterised by coarse sands in the ND, which grade rapidly into dark brown silty sands and is followed by coarse sands at ~7.6–7.2 ka cal BP (531–512 cm; Fig. 2; Table 2). The first dark brown/black peat level appears in the sequence from ~7.2 ka cal BP to 6.1 ka cal BP (512–465 cm; Fig. 2; Table 2). The pre-peat phase shows similar characteristics to those observed in the 8.2 ka cal BP event, with moderately positive Al/Ti and Mn/Fe ratios, low LOI and MS, and the sporadic presence in macro-charcoals, and lower PC1 values (Fig. 6). These results suggest the formation of Mn oxide (oxidizing conditions) and low water base levels with drier and warmer conditions at this time (~7.6–7.2 ka cal), like in the Mediterranean area (Jalut et al., 2000) and northern Iberian lakes (Jalut et al., 2010; Carrión et al., 2010; Moreno et al., 2011).

The occurrence of peat, lower Al/Ti and Mn/Fe ratios, and higher LOI values (7 and 6, Fig. 6; ~6.9–6.8 ka, and 6.6 ka cal BP, respectively) suggest low water renewal rates and anoxic conditions (Davison, 1993; Dean et al., 1997) leading to the establishment of a mire after ~7.2 ka cal BP (Fig. 6). This peat coincided with a low MS (Fig. 6) and the high probability of an event (Fig. 3). At the same time, the PC1 values increased, while the PC2, PC3, and PC4 values decreased (Fig. 6). This part of the sequence at ~7.2–6.1 ka cal BP is characterised by a slight reduction in the detrital input (low PC2 values; Fig. 6), suggesting slope stabilisation and soil recovering at the time of the presence of peat-type vegetation in the ND (López-Sáez et al. 2020). We interpret this as a period of propitious insolation (in summer), under a relatively warm and regionally humid period. Peat accumulation in the ND informs about a palustrine-like environment (Turu et al., 2018), suggesting episodes of shallow water levels (López-Merino et al., 2010, 2011; Magny et al., 2013; Pontevedra-Pombal et al., 2017, 2019; Camuera et al., 2018). The age-depth model of the core (Fig. 2) suggests that these events correlate with the so-called Holocene Climate Optimum, a well-known period that

was humid and warm in the southwestern Mediterranean (Roberts et al., 2004; Carrión et al., 2010). Millennial oscillations changed at 7000 cal BP in the Early and Mid-Holocene divide (Domínguez-Villar et al., 2017). Notably, a climatic latitudinal anti-phase during the Holocene possibly was modulated by an NAO-like climate mechanism (Vannière et al., 2011; Rius et al., 2011).

The terrigenous input to Navamuño declined between ~5.9 ka cal BP and 5.6 ka cal BP along with the values of MS, PC1, PC2, and PC4 and was accompanied by an increase in the fine grain-sized fraction (very fine sand; Fig. 2; Table 2). This suggests progressive reforestation (Figs. 3 and 6). Low Mn/Fe ratio values indicate the presence of a high water level, which probably drained along a braided to meandering channel system in the ND (Turu et al., 2018).

Van der Knaap and van Leeuwen (1995) indicate that deforestation changed the landscape of the Serra da Estrela (ICS) at around 6–6.3 ka cal BP. In Navamuño, the occurrence of sedimentary charcoals at depths of 4.5–4.75 m (6.2 ka cal BP; Fig. 6) in an inverse grain-size grading layer (coarsening upward trend; Turu et al., 2018) was interpreted as a product of human-induced palaeoburnings in studies conducted by Riera and Turu (2011). The palaeofires that are inferred from the pollen diagram of La Molina peat bog in Puente Viesgo in Cantabria (Fig. 7a) are accompanied by continuous sedimentary charcoal records at 6–6.5 ka cal BP (Pérez-Obiol et al., 2016), which are similar to those observed in the core from Navamuño. These results show the importance of human-influenced fire activity in the Puente Viesgo region during different cultural phases. For Connor et al. (2019), the evidence indicates a first wave of Neolithic burning promoting an increasing in the vegetation openness, woodland diversity around settlements between 7.5 and 5.5 ka cal. BP.

7.6.2. Extra-basin gains

Nevertheless, the trend in the principal components varies at 7.5 ka cal BP and coincided with the switch of non-Saharan dust (NSD) influx (Fig. 6) to more frequent Saharan dust (SD) events (Fig. 6), accordingly to Le Roux et al. (2012) conclusions. Geochemically overprinted, Cl, S, Cu, and several other metals exert a progressive influence on the observed behaviour in PCA (Fig. 6); this occurs at 6.8 ka (PC1), then at 6.5 ka (PC2), at 6.4 ka (PC3) and finally at 5.8 ka (PC4). MS (Fig. 6; number 1) and LOI (number 5) both peaked when the dust supply changed from the more light-associated elements (K, Cu, Sr, Si, Cl, S) of PC1 to the metals (Zn, V, Zr, Cu, Pb, Fe, Ni) of PC2 and the Ni, Zn, Br, Cu associated with PC3 until the prominent Cu peak at 5.8 ka cal BP (Fig. 3) is reached. High V and Hg concentrations were observed in Roñanzas (Fig. 7b), offering evidence of volcanic activity starting at 6.8 ka cal BP, which culminates at 5.7 ka cal BP, when the probability of an event in Navamuño was at a maximum (Fig. 3). In Villarquemado (Fig. 7a), an MS peak is observed around ~6 ka cal BP, also a decrease in Ca, Sr, while the Zr trend changes (González-Sampériz et al., 2020; Supplementary Appendix A4). In Marboré lake (Oliva-Urcía et al., 2018; Supplementary Appendix A4) and in the Enol lake (Moreno et al., 2011; Supplementary Appendix A4), an MS peak also occurs around ~6 ka cal BP. The geographical position of Navamuño, Enol and Roñanzas match with an N-S direction origin for the ash influx; besides, the geographical position of Marboré and Villarquemado is a NE-SW direction (also Estaña; Morellón et al., 2012; Supplementary Appendix A4). Both directions point to the Calatreva volcanic field. However, Poblete-Piedrabuena et al. (2019) identified volcanic activity in the Columba volcano in Granátula de Calatrava (Castilla-La Mancha, Fig. 7b), just before 6.27 ± 0.438 ka using OSL (Optically Stimulated Light). For Roñanzas, only favourable atmospheric patterns could be under the Columba Volcano influx. Based on the current synoptic situations over Iberia (Petisco de Lara, 1996), over ~50 cases, occurrence 7.2 %, 2 %, and 12.5 % ash dissemination in Navamuño, Roñanzas/Enol, and Villarquemado/Marboré, respectively, can be attributed to the Calatrava volcanic field.

7.7. The Mid-Holocene ending (~5.9–4.2 ka cal BP)

At around 5.6–5.5 ka cal BP, the Al/Ti and Mn/Fe ratios increased again, while the MS, LOI, and PC1 values sharply decreased (Fig. 6), probably owing to a change in the sedimentation dynamics and the deposition of a layer of coarse sand (442–435 cm; Fig. 2; Table 2). Coinciding with Bond event 4 (Bond et al., 1997, 2001) and the establishment of drier conditions across the Mediterranean (Jalut et al., 2000), many palaeoclimate records show changes in the seasonality of precipitation around ~5.5 ka cal BP, mainly associated with a decrease in insolation maxima and a reorganisation of the atmospheric circulation (Jalut et al., 2010; Magny et al., 2013; Zielhofer et al., 2017b). The aforecited layer between 442 and 435 cm results from this palaeoenvironment change in the ND. Notably, the values of lithogenic elements (Ti, K, Ca, Co, Rb, Zr) present within the core decrease until ~5.3 ka cal BP (Fig. 3), indicating drier conditions (Kylander et al., 2011). Special arid conditions in the NW Iberian Peninsula 5126 years ago (U/Th age series) (Cova Arcoia, Fig. 7a) are inferred from the ESP05 stalagmite (Railsback et al., 2011). Based on speleothem data (El Refugio cave, Fig. 7a), the Mid-Holocene aridity (Jalut et al., 2000) preceded the onset of the Mediterranean climate at 5.3 ka BP in southern Iberia (Walczak et al. 2015). From ~5.5 to 4.3 ka cal BP (414–392 cm), the probability of an event was high at 4.9 ka cal BP (Fig. 3), and the sedimentary system appears to have stabilised, with decreasing Al/Ti and Mn/Fe ratios, suggesting the existence of overbank deposits (black silts; Figs. 2 and 6; Table 2) that may come from floodings. A peak in the LOI (number 4) could explain the dark tonality of these silts at ~4.9 ka cal BP as the dark-brown colour is enhanced by the presence of organic matter (Koinig et al., 2003; Kylander et al., 2011). However, S and P increased in this period, which coincides with an increase in the dust loading from the Sahara between 7 ka cal BP and 4.5 ka cal BP (Rodrigo-Gámiz et al., 2011). At the end of this dusty period, burning occurred at ~4.4 ka cal BP, as inferred from the presence of macro-charcoal in the ND (Fig. 6).

The final part of the Mid-Holocene at ~4.2 ka cal BP is by sands characterised and an increase of the sedimentary rate (0.58 mm/yr) (Fig. 2; Table 2). Notably, the terrigenous input, LOI, and Al/Ti ratio decreased (Fig. 6). Although these changes were subtle and may correlate with the arid and cooler climate event of Bond 3 (Bond et al., 1997, 2001), the consequences are evident in the reconstruction of in the ND at around 4.2 ka cal BP, from a sharp LOI decrease (Turu et al., 2018) and a reduction in the computed palaeotemperatures (Fig. 3). In the ND, a decline in biomass burning is inferred from the absence of macro-charcoals (Fig. 6). This event has been recognised as a marked aridification phase in the Mediterranean region (Jalut et al., 2000), particularly in the ICS; the consequences of which are reflected in the archaeological record detailing the collapse of the Chalcolithic agrarian landscape (Fabián et al., 2006; Lillios et al., 2016; Blanco-González et al., 2018). Despite being a very arid event, the XRF data do not change in the Mn/Fe ratio (Fig. 6), suggesting forming a permanent broad floodplain in the ND.

The climatic influence of the North Atlantic circulation produced in Bassa Nera (Fig. 7a; Central Pyrenees) shifts from deciduous forest to coniferous taxa at 4200 cal yr BP, which is linked with flooding between 4500 cal yr BP and 3900 cal yr BP (Garcés-Pastor et al., 2017). A fall in pine population is observed at 4707 ± 136 cal yr BP at Lagoa Traversa (Fig. 7a) and in SW Portugal (Mateus, 1992). In Lucenza (Fig. 7a; Sierra de Courel, NW Iberia; Santos-Fidalgo et al., 2000), human activity starts at 4622 ± 200 cal yr BP, and falls in pine taxa occurs later, at around 2203 ± 154 cal yr BP. Human activity is evident at La Mata (Fig. 7a) around 3961 ± 136 cal yr BP, but some indicators have been observed as early as 4500 cal yr BP (Jalut *pers. comm.*).

7.8. The Late-Holocene (~4.2 ka cal BP to present)

Pérez-Obiol et al. (2011) emphasised the absolute predominance of

Scots pine forests in Sierra de Guadarrama (central-eastern ICS) since the early Mid-Holocene period. Human activity has been recognised in Sierra de Béjar since 4 ka cal BP (Atienza, 1993; Rubiales et al., 2007), indicating the likelihood of palaeoburning. At the same time, a drastic fall in arboreal pollen occurred at 4142–4104 cal yr BP in Sierra de Guadarrama (Franco-Múgica et al., 1998), which is probably due to an increase in the aridity under strong continental climatic conditions (Franco-Múgica et al., 1998). The spread of human activity from the valleys to the high mountains originated in the agrarian Chalcolithic landscape (López-Sáez et al., 2014). The meagre sedimentation rates in La Mata (SW Cantabrian mountains; Jalut et al., 2010) ended at 3900 cal yr BP, suggesting a limited water supply and possible hiatus.

The early Late-Holocene (~4.2–3.2 ka cal BP) was a relatively stable period in the ND, during which the Al/Ti and Mn/Fe ratios, along with the values of MS and most lithogenic and biogenic elements, were low. The LOI increased, culminating in a peak at ~3.2–3.1 ka cal BP (28 %; number 3; Fig. 6), at 325–315 cm (Fig. 2). Le Roux et al. (2012) indicated the stabilisation of the dust influx over Europe posterior to 5 ka cal BP; however, the S peak at 3.2 ka cal BP (Fig. 3) may point to a later input of dust reaching the ND, coinciding with higher values of PC2, P, S, and Ni (Figs. 3 and 6). Additionally, a rapid transition from coarse to dark brown silts occurred between 371 cm and 315 cm (Fig. 2; Table 2). These data suggest episodic flooding in the ND, thus, increasing the amount of organic matter. Subsequently, macro-charcoal peaks (6.8 mm^2/g) for the whole Navamuño sequence at ~3.0 ka cal BP coincide with an increase in the Al/Ti ratio and PC3 values and a decrease in the PC1, PC2, and PC4 values (Fig. 6). The values of most lithogenic elements (Rb, NB, Zr, Sr, and Fe) decreased at ~3.0 ka cal BP (Fig. 3). These changes coincide with the last communities of the Late Bronze Age in the western Gredos range (López-Sáez et al., 2009, 2014, 2016).

However, the previous trend abruptly changed at ~2.8 ka cal BP, indicated by the decrease in the Al/Ti and Mn/Fe ratios and the LOI values, the disappearance of macro-charcoals, and a minimum in PC1, PC2, and PC3 (Fig. 6). Only the PC4 shows an increase in Cl, with the high values maintained until the end of the sequence (Figs. 3 and 6). Cl is a significant atmospheric trace constituent, and at 2.8 ka cal BP starts a pervasive oceanic influence in the western ICS carrying Cl-rich aerosol from the Atlantic Ocean. A colder period around 2.8 ka cal BP is in the ND (Fig. 3), probably associated with the Bond 2 event (Bond et al., 2001) and at the onset of the Iron Age in the western ICS (López-Sáez et al., 2014). PC4 (Figs. 3 and 6) increased at ~2800 cal BP and maintained the high values until the end of the sequence. Cl is generally present in sediments formed during humid periods or under influx from the Atlantic Ocean, such as between the 2.8 ka cal BP event and the Ibero-Roman humid period. Wetter conditions facilitated the development of productive activities (agriculture and livestock) and resulted in an increase in the deforestation of the landscape in the Béjar range (Abel-Schaad and López-Sáez, 2013; López-Sáez et al., 2016). Such wetter conditions agree with the higher water tables reported during this event by other mires in the western ICS, northern Iberian Plateau, and northwestern Iberia (Blanco-González and López-Sáez et al., 2013; Pontevedra-Pombal et al., 2019). Of the different soil types and sedimentary environments, peat provides the largest terrestrial Cl reservoir (Dimmer et al., 2001). Shallow wetlands are a suitable medium for forming and storing organically bound Cl (Keppler and Biester, 2003). The primary role of peat in the biochemical cycle of Cl results from its high storage capacity and the permanent anoxic conditions that predominate in mires (Pontevedra-Pombal et al., 2017). Therefore, the affinity of peat to capture atmospheric Cl explains the high values since the inception of peat at ~2100 cal BP (Schofield et al., 2010). Moisture decrease in the mire subsequently entails mineralisation of peat and the concentration of organically bound Cl due to mass loss. Once formed at ~2800 cal BP, the amount of Cl remained high in the Navamuño sequence, without considerable variation, indicating that organic Cl was preserved under these specific redox conditions, rendering dechlorination relatively slow processes.

The last three millennia of the geochemical record (~2800 cal BP to present) were highly variable, with alternating periods of high and low Mn/Fe ratios and high LOI (numbers 2 and 1; Fig. 6). However, a longer and smoother dust regime started at 2 ka (Le Roux et al., 2012).

The first peak in LOI (Fig. 6) coincided with the Little Ice Age (LIA; ~600–100 cal BP). The probability of an event was high when the levels of P peaked at 1.2 ka cal BP (Fig. 3), which occurred during dry phases such as the Early Medieval Cold Episode (EMCE; ~1500–1000 cal BP). The second LOI peak correlates with a wet phase such as the Ibero-Roman humid period (IRHP; ~2800–1500 cal BP). An arid to moist shift occurs in the ICS during the Dark Ages Cold Period (McDermott et al., 2001) at 0.9 ka cal BP (Sánchez-López et al., 2016). This dry to wet shift phase around ~0.9 ka cal BP show decreasing trends in the PC1 and PC3 values and increasing trends in the PC2 values, while the wet phases show the opposite (Fig. 6); all geochemical elements changed sharply (Fig. 3), coinciding with the Late Medieval Warm Episode (LMWE; ~1000–600 cal BP). These climatic periods during the Middle Ages, particularly in the ICS (Blanco-González et al., 2015), are documented in the Iberian bibliography (Oliva et al., 2017). It is interesting to note the formation of a new peat layer (254–135 cm) during the Ibero-Roman humid period ~2100 cal BP (Fig. 2; Table 2), which was active until the end of the LMWE that occurred at ~600 cal BP, before disappearing because of the cold and arid conditions in the LIA at ~400 cal BP (Fig. 3).

8. Conclusions

The Navamuño core provides a continental record of the entire Late Glacial–Holocene period in western and central Iberia, despite the variability in its sedimentary rate. However, the most substantial evidence of palaeoenvironmental change is presented in the sequence produced in this study.

1. The Oldest Dryas (~15.6–14.7 ka cal BP) of the sequence is part of the glacial retreat phase of the CH glacier. The ND was an amictic lake dammed by the resulting lateral moraine. A maximum flooding surface at ~15.6 ka cal BP match with a hydroclimate reorganisation after Heinrich Event 1
2. During cold periods, permanent floods under somewhat oceanic climate conditions are observed in the Older Dryas (~14–13.4 ka cal BP) and the Intra-Allerød Cold Period (~13.1–12.9 ka cal BP), low organic matter productivity and a near absence of fire-charred remains.
3. Instead of warm episodes, LOI progressively increases, such as the Bølling (~14.7–14 ka cal BP), alongside fire frequency such as the Allerød (~12.9–12.6 ka cal BP) sub-interstadial. However, the GI-1c (~13.4–13.1 ka cal BP) is barely recognizable and only when comparing episodes, an increase in the principal component (PC2) occurred during the three warm periods.
4. The atmospheric pattern over Iberia entailed remote ash and dust sources from the south to move northwards. Ash infux may come from the Columba volcano in southcentral Iberia, which erupted around 13.8 ka cal BP. We attribute to this eruption the strong decrease for PC4 and peaks in Rb and Zn. Nonetheless, enhanced the P, S and Ca amounts in the ND starting at 12.8 ka cal BP may have a source in the Asian deserts.
5. During the YD stadial ~12.6–11.7 ka cal BP, organic matter production increases parallel to fire activity and desiccation in the ND at the end of this stadial. This advocate for a moist/cold to dry/warm climate structure for the YD. At the Early Holocene, the area transformed into a marshy area subjected to subsidence and tectonic instability between ~11.3–10.95 ka cal BP.
6. At the early Pre-boreal (~11.7–11.3 ka cal BP), significant fire activity affected the ND accordingly to the westernmost ICS's data. A relative high Cu peak at 11.4 ka cal BP suggests volcanic ash blowing over the ND. During the late Pre-boreal

~11.3–10.95 ka cal BP a wide floodplain covering the ND under the influence of brief spells from the Atlantic as inferred from Cl peaks at ~10.9–10.8 ka cal BP and 10.2 ka cal BP. At the Early Holocene, the abrupt climate event at ~9.3 ka cal BP started cooler and wetter conditions and frequent flooding activity in the ND.

7. At the early Mid-Holocene, all metals peak at ~9.0–8.4 ka cal BP, when a new dusty and arid period prevailed before the cold event at 8.2 ka cal BP. Warmer conditions somewhat drier are inferred from low water levels at ~7.6–7.2 ka cal BP, the ND transformed in a mire.
8. During the Holocene Climatic Optimum significant variation in the principal components occurs at 7.5 ka cal BP, attributed to more frequent Saharan dust inputs. Soils may form on the slopes around the ND since detrital input is reduced at ~7.2–6.1 ka cal BP. Overprinted ash influx from volcanic activity in the south-central Iberia at 6.27 ± 0.438 ka led to progressive behaviour changes in the principal components at 6.7 ka, 6.5 ka, 6.4 ka and 5.8 ka.
9. An early human impact at 6.2 ka is suggested from charred remains and inverse grain-size grading in the floodplain sediments. Nevertheless, reforestation accompanied by significant water levels at ~5.9–5.6 ka cal BP covers the ND along a braided to meandering channel system. Drier conditions at ~5.5 ka cal BP coincided with the Bond event 4. S and P peaked at ~4.9 ka cal BP due to an increase in the dust loading from Sahara until 4.5 ka cal BP. P/Cl pulses and macro-charcoal peaks match at 8.0 ka, 5.8, 4.5, and 3.0 ka cal BP.
10. At the early Late-Holocene (~4.2–2.8 ka cal BP), a decline in biomass advocates for colder and drier climate at ~4.2 ka cal BP. The S peak at 3.2 ka was probably the result of a new dust input into the ND. The pervasive presence of oceanic aerosols in the last three millennia allowed the formation of a Cl-rich peat layer during the Ibero-Roman humid period ~2100, before a changing around ~400 cal BP toward colder drier conditions at the LIA period.

Geochemically speaking, a decrease in the Cl content suggests a reduction in the oceanic influence when P increased, and Al/Ti peaked, indicating more frequent dusty episodes from the Sahara and progressive warming that entailed frequent palaeofires.

Declaration of Competing Interest

The authors declare that they have no known competing financial interests or personal relationships that could have appeared to influence the work reported in this paper.

Acknowledgements

This study was funded by the LATESICE-CGL2016-78380-P, FINICES- PID2020-117685 GB-I00 and MED-REFUGIA-RTI2018-101714-B-I00 (Plan Nacional I + D + I, Spanish Ministry of Science, Innovation and Universities) projects. This study was also funded by the OROMEDREFUGIA project (P18-RT-4963) from the Andalusian Office of Economy and Knowledge. Luelmo Lautenschlaeger was funded by the Spanish Ministry of Education, Culture, and Sports (FPU16/00676). We sincerely thank Dr. Guy Jalut for the constructive and helpful comments that improved our original draft. We would also like to sincerely thank Professor Eneko Iriarte, University of Burgos, Spain, for his help and advice in interpreting the geochemical records. We also thank the editor and the anonymous reviewers for their helpful comments and constructive suggestions that have significantly improved this manuscript.

Appendix A. Supplementary data

Supplementary data to this article can be found online at https://doi.org/10.1016/j.catena.2021.105689.

References

Abel-Schaad, D., López-Sáez, J.A., 2013. Vegetation changes in relation to fire history and human activities at the Peña Negra mire (Béjar Range, Iberian Central Mountain System, Spain) during the past 4.000 years. Veget. Hist. Archaeobot. 22, 199–214. https://doi.org/10.1007/s00334-012-0368-9.

Abel-Schaad, D., Iriarte, E., López-Sáez, J.A., Pérez-Díaz, S., Sabariego, S., Cheddadi, R., Alba-Sánchez, F., 2018. Are Cedrus atlantica forests in the Rif Mountains of Morocco heading towards local extinction? Holocene 28, 1023–1037 https://doi.org/10.1177%2F0959683617752842.

AEMET/IPMA, 2011. Atlas Climático Ibérico-iberian Climate Atlas. Agencia Estatal de Meteorología (AEMET) and Instituto Português do Mar e da Atmosfera (IPMA), Madrid.

Allard, J.L., Hudhes, P.D., Woodward, J.C., 2021. Heinrich Stadial aridity forced Mediterranean-wide glacier retreat in the last cold stage. Nat. Geosci. 14, 197–205. https://doi.org/10.1038/s41561-021-00703-6.

Alley, R., 2000. The Younger Dryas cold interval as viewed from central Greenland. Quat. Sci. Rev. 19, 213–226. https://doi.org/10.1016/S0277-3791(99)00062-1.

Alley, R.B., Mayewski, P.A., Sowers, T., Stuiver, M., Taylor, K.C., Clark, P.U., 1997. Holocene climate instability: a prominent, widespread event 8200 yr ago. Geology 25, 483–486. https://doi.org/10.1130/0091-7613(1997)025<0483:HCIAPW>2.3.CO;2.

Aranbarri, J., González-Sampériz, P., Valero-Garcés, B.L., Moreno, A., Gil-Romera, G., Sevilla, M., García-Prieto, E., di Rita, F., Mata, M.P., Morellón, M., Magri, D., Rodríguez-Lázaro, J., Carrión, J.S., 2014. Rapid climatic changes and resilient vegetation during the Lateglacial and Holocene in a continental region of southwestern Europe. Glob. Planet. Change 114, 50–65. https://doi.org/10.1016/j.gloplacha.2014.01.003.

Atienza, M., 1993. Evolución del paisaje vegetal en las Sierras de Béjar y Francia durante el Holoceno, a partir del análisis polínico. Ph.D. Thesis. Alcalá de Henares Univ, Spain.

Bal, M.C., Pèlachs, A., Pérez-Obiol, R., Julia, R., Cunill, R., 2011. Fire history and human activities during the last 3300 cal yr BP in Spain's Central Pyrenees: the case of the Estany de Burg. Palaeogeogr. Palaeoclimatol. Palaeoecol. 300 (1–4), 179–190. https://doi.org/10.1016/j.palaeo.2010.12.023.

Baldini, L.M., McDermott, F., Baldini, J.U.L., Arias, P., Cueto, M., Fairchild, I.J., Hoffmann, D.L., Mattey, D.P., Müller, W., Nita, D.C., Ontañón, R., García-Moncó, C., Richards, D.A., 2015. Regional temperature, atmospheric circulation, and sea-ice variability within the Younger Dryas Event constrained using a speleothem from northern Iberia. Earth Planet. Sci. Lett. 419, 101–110. https://doi.org/10.1016/j.epsl.2015.03.015.

Bartolomé, M., Moreno, A., Sancho, C., Stoll, H.M., Cacho, I., Spötl, C., Belmonte, A., Edwards, R.L., Cheng, H., Hellstrom, J.C., 2015. Hydrological change in southern Europe responding to increasing north Atlantic overturning during Greenland stadial 1. Proc. Natl. Acad. Sci. 112, 6568–6572. https://doi.org/10.1073/pnas.1503990112.

de Beaulieu, J.L., Brugiapaglia, E., Joannin, S., Guiter, F., Zanchetta, G., Wulf, S., Peyron, O., Bernardo, L., Didier, J., Stock, A., Rius, D., Magny, M., 2017. Lateglacial-Holocene abrupt vegetation changes at Lago Trifoglietti in Calabria, Southern Italy: The setting of ecosystems in a refugial zone. Quat. Sci. Rev. 158, 44–57. https://doi.org/10.1016/j.quascirev.2016.12.013.

Björck, S., et al., 1997. The Preboreal oscillation around the Nordic Seas: terrestrial and lacustrine responses. J. Quat. Sci. 12, 455–465. https://doi.org/10.1002/(SICI)1099-1417(199711/12)12:6<455::AID-JQS316>3.0.CO;2-S.

Blaauw, M., Christen, J.A., Mauquoy, D., van der Plicht, J., Bennett, K.D., 2007. Testing the timing of radiocarbon-dated events between proxy archives. The Holocene 17, 283–288.

Blaauw, M., 2010. Methods and code for classical age-modelling of radiocarbon sequences. Quat. Geochron. 5, 512–518. https://doi.org/10.1016/j.quageo.2010.01.002.

Blanco-González, A., López-Sáez, J.A., 2013. Dynamics of pioneer colonization in the Early Iron Age in the Duero basin (Central Iberia, Spain): Integrating archaeological and palynological records. Environ. Archaeol. 18, 102–113. https://doi.org/10.1179/1461410313Z.00000000025.

Blanco-González, A., Lillios, K.T., López-Sáez, J.A., Lee-Drake, B., 2018. Cultural, demographic and environmental dynamics of the Copper and Early Bronze Age in Iberia (3300–1500 BC): towards an interregional multi-proxy comparison at the time of the 4.2 ky BP event. J. World Prehist. 31, 1–79. https://doi.org/10.1007/s10963-018-9113-3.

Blanco-González, A., López-Sáez, J.A., Alba-Sánchez, F., Abel-Schaad, D., Pérez-Díaz, S., 2015. Medieval landscapes in the Spanish Central System (450–1350): a palaeoenvironmental and historical perspective. J. Mediev. Iber. Stud. 7, 1–17. https://doi.org/10.1080/17546559.2014.925135.

Bond, G., Kromer, B., Beer, J., Muscheler, R., Evans, M.N., Showers, W., Hoffmann, S., Lotti-Bond, R., Hajdas, I., Bonani, G., 2001. Persistent solar influence on North Atlantic climate during the Holocene. Science 294, 2130–2136. https://doi.org/10.1126/science.1065680.

Bond, G., Showers, W., Cheseby, M., Lotti, R., Almasi, P., de Menocal, P., Priore, P., Cullen, H., Hajdas, I., Bonani, G, 1997. A pervasive millennial-scale cycle in North

Atlantic Holocene and glacial climates. Science 278, 1257–1266. https://doi.org/10.1126/science.278.5341.1257.
Bos, J.A.A., van Geel, B., van der Plicht, J., Bohncke, S.J.P., 2007. Preboreal climate oscillations in Europe: Wiggle-match dating and synthesis of Dutch high-resolution multi-proxy records. Quat. Sci. Rev. 26, 1927–1950. https://doi.org/10.1016/j.quascirev.2006.09.012.
Burjachs, F., Jones, S.E., Giralt, S., López, Fernández, de Pablo, J., 2016. Lateglacial to Early Holocene recursive aridity events in the SE Mediterranean Iberian Peninsula: The Salines playa lake case study. Quat. Int. 403, 187–200. https://doi.org/10.1016/j.quaint.2015.10.117.
Calvert, S.E., Pedersen, T.F., 2007. Elemental Proxies for Palaeoclimatic and Palaeoceanographic Variability in Marine Sediments: Interpretation and Application. In: Claude, H., Anne De, V. (Eds.), Developments in Marine Geology. Elsevier, pp. 567–644.
Camarero, I., Catalan, J., 2012. Atmospheric phosphorus deposition may cause lakes to revert from phosphorus limitation back to nitrogen limitation. Nat. Commun. 3, 1118. https://doi.org/10.1038/ncomms2125.
Camarero I., 2017. Atmospheric chemical loadings in the high mountain: current forcing and legacy pollution. In J. Catalan, J. M. Ninot and M. M. Aníz (eds.), High Mountain Conservation in a Changing World, Advances in Global Change Research 62, 325-341.
Camuera, J., Jiménez-Moreno, G., Ramos-Román, M.J., García-Alix, A., Toney, J.L., Scott Anderson, R., Jiménez-Espejo, F., Bright, J., Webster, C., Yanes, Y., Carrión, J.S., 2019. Vegetation and climate changes during the last two glacial-interglacial cycles in the Western Mediterranean: A new long pollen record from Padul (southern Iberian Peninsula). Quat. Sci. Rev. 205, 86–105. https://doi.org/10.1016/j.quascirev.2018.12.013.
Camuera, J., Jiménez-Moreno, G., Ramos-Román, M.J., García-Alix, A., Toney, J.L., Scott Anderson, R., Jiménez-Espejo, F., Kaufman, D., Bright, J., Webster, C., Yanes, Y., Carrión, J.S., Ohkouchi, N., Suga, H., Yamame, M., Yokoyama, Y., Martínez-Ruiz, F., 2018. Orbital-scale environmental and climatic changes recorded in a new ~200,000-year-long multi-proxy sedimentary record from Padul, southern Iberian Peninsula. Quat. Sci. Rev. 198, 91–114. https://doi.org/10.1016/j.quascirev.2018.08.014.
Carcaillet, C., Bergman, I., Delorme, S., Hornberg, G., Zackrisson, O., 2007. Long-term fire frequency not linked to prehistoric occupations in northern Swedish boreal forest. Ecology 88, 465–477. https://doi.org/10.1890/0012-9658(2007)88[465:LFFNLT]2.0.CO;2.
Carrasco, R.M., Pedraza, J., Domínguez-Villar, D., Muñoz-Rojas, J., 2008. El glaciarismo Pleistoceno de la Sierra de Béjar (Gredos occidental, Salamanca, España): nuevos datos para precisar su extensión y evolución. Bol. R. Soc. Esp. Hist. Nat. Sec. Geol. 102, 35–45.
Carrasco, R.M., Pedraza, J., Domínguez-Villar, D., Villa, J., Willenbring, J.K., 2013. The plateau glacier in the Sierra de Béjar (Iberian Central System) during its maximum extent. Reconstruction and chronology. Geomorphology 196, 83–93. https://doi.org/10.1016/j.geomorph.2012.03.019.
Carrasco, R.M., Pedraza, J., Domínguez-Villar, D., Willenbring, J.K., Villa, J., 2015a. Sequence and chronology of the Cuerpo de Hombre palaeoglacier (Iberian Central System) during the last glacial cycle. Quat. Sci. Rev. 129, 163–177. https://doi.org/10.1016/j.quascirev.2015.09.021.
Carrasco, R.M., Sánchez, J., Muñoz-Martín, A., Pedraza, J., Olaiz, A.J., Ruiz-Zapata, B., Abel-Schaad, D., Merlo, O., Domínguez-Villar, D., 2015b. Caracterización de la geometría de la depresión de Navamuño (Sistema Central Español) aplicando técnicas geofísicas. Geogaceta 57, 39–42.
Carrasco, R.M., Turu, V., Pedraza, J., Muñoz-Martín, A., Ros, X., Sánchez, J., Ruiz-Zapata, B., Olaiz, A.J., Herrero-Simón, R., 2018. Near surface geophysical analysis of the Navamuño depression (Sierra de Béjar, Iberian Central System): Geometry, sedimentary infill and genetic implications of tectonic and glacial footprint. Geomorphology 315, 1–16. https://doi.org/10.1016/j.geomorph.2018.05.003.
Carrión, J.S., 2002. Patterns and processes of Late Quaternary environmental change in a montane region of southwestern Europe. Quat. Sci. Rev. 21, 2047–2066. https://doi.org/10.1016/S0277-3791(02)00010-0.
Carrión, J.S., Fernández, S., González-Sampériz, P., Gil-Romera, G., Badal, E., Carrión, Y., López-Merino, L., López-Sáez, J.A., Fierro, E., Burjachs, F., 2010. Expected trends and surprises in the Late Glacial and Holocene vegetation history of the Iberian Peninsula and Balearic Islands. Rev. Palaeobot. Palynol. 162, 458–475. https://doi.org/10.1016/j.revpalbo.2009.12.007.
Catuneanu, O., 2006. Principles of Sequence Stratigraphy. Elsevier Science, Amsterdam, Netherlands, p. 375.
Chesworth, W., Martínez-Cortizas, A., García-Rodeja, E., 2006. Redox-pH approach to the geochemistry of the Earth's land surface, with application to peatlands. In: Martini, I.P., Martínez-Cortizas, A., Chesworth, W. (Eds.), Peatlands: Evolution and Records of Environmental and Climate Changes. Elsevier, Amsterdam, pp. 175–196.
Cohen, A.S., 2003. Palaeolimnology: The history and Evolution of Lake Systems. Oxford University Press, New York.
Connor, S.E., Araújo, J., van der Knapp, W.O., van Leeuwen, J.F.N., 2012. A long-term perspective on biomass burning in the Serra da Estrela. Portugal. Quat. Sci. Rev. 55, 114–124. https://doi.org/10.1016/j.quascirev.2012.08.007.
Connor, S.E., Vannière, B., Colombaroli, D., Scott Anderson, R., Carrión, J.S., Ejarque, A., Gil-Romera, G., González-Sampériz, P., Hoefer, D., Morales-Molino, C., Revelles, J., Schneider, H., van der Knaap, W.O., van Leeuwen, J.F.N., Woodbridge, J., 2019. Humans take control of fire-driven diversity changes in Mediterranean Iberia's vegetation during the mid-late Holocene. Holocene 29, 886–901. https://doi.org/10.1177/0959683619826652.
Croudace, I.W., Löwemark, L., Tjallingii, R., Zolitschka, B., 2019. Current perspectives on the capabilities of high resolution XRF core scanners. Quat. Int. https://doi.org/10.1016/j.quaint.2019.04.002.
Dai, Q., Chiao, J., 2019. Quantify the atmospheric methyl bromide source with boxes models and data from the ground-based measurement station of global monitoring division (NOAA). AGU Fall Meeting Abstracts A43P–A2029. https://ui.adsabs.harvard.edu/abs/2019/AGUFM.A4P2928D.
Dall'Osto, M., Harrison, R.M., Highwood, E.J., O'Dowd, C., Ceburnis, D., Querol, X., Achterberg, E.P., 2010. Variation of the mixing state of Saharan dust particles with atmospheric transport. Atmos. Environ. 44 (2010), 3135–3146.
Daniau, A.L., Sánchez-Goñi, M.F., Beaufort, L., Laggoun-Défarge, F., Loutre, M.F., Duprat, J., 2007. Dansgaard-Oeschger climatic variability revealed by fire emissions in southwestern Iberia. Quat. Sci. Rev. 26, 1369–1383. https://doi.org/10.1016/j.quascirev.2007.02.005.
Davison, W., 1993. Iron and manganese in lakes. Earth-Sci. Rev. 34, 119–163. https://doi.org/10.1016/0012-8252(93)90029-7.
de Vicente, G., Cloetingh, S., Van Wees, J.D., Cunha, P.P., 2011. Tectonic classification of Cenozoic Iberian foreland basins. Tectonophysics 502, 38–61. https://doi.org/10.1016/j.tecto.2011.02.007.
Dean, W.E., Gardner, J.V., Piper, D.Z., 1997. Inorganic geochemical indicators of glacial-interglacial changes in productivity and anoxia on the California margin. Geochim. Cosmochim. Acta 61, 4507–4518. https://doi.org/10.1016/S0016-7037(97)00237-8.
Deines, F., 1980. The isotopic composition of reduced organic carbon. In: Fritz, F., Fontes, J.C. (Eds.), Handbook of Environmental Isotope Geochemistry, vol. 1. Elsevier, Amsterdam, pp. 329–406.
Demory, F., Oberhansli, H., Nowaczyk, N.R., Gottschalk, M., Wirth, R., Naumann, R., 2005. Detrital input of early diagenesis in sediments from Lake Baikal revealed by rock magnetism. Glob. Planet. Change 46, 145–166. https://doi.org/10.1016/j.gloplacha.2004.11.010.
Denton, G.H., Alley, R.B., Comer, G.C., Broecker, W.S., 2005. The role of seasonality in abrupt climate change. Quat. Sci. Rev. 24, 1159–1182. https://doi.org/10.1016/j.quascirev.2004.12.002.
Denton, G.H., Broecker, W.S., Alley, R.B., 2006. The mystery interval 17.5 to 14.5 kyrs ago. PAGES News 14, 14–16. https://doi.org/10.22498/pages.14.2.14.
Dimmer, C.H., Simmonds, P.G., Nickless, G., Bassford, M.R., 2001. Feurdean Environ. 35, 321–330.
Domínguez-Villar, D., Carrasco, R.M., Pedraza, J., Cheng, H., Edwards, R.L., Willenbring, J.K., 2013. Early maximum extent of palaeoglaciers from Mediterranean mountains during the last glaciation. Sci. Rep. 3 (2034), 1–6. https://doi.org/10.1038/srep02034.
Domínguez-Villar, D., Wang, X., Krklec, K., Cheng, H., Edwards, R.L., 2017. The control of the tropical North Atlantic on Holocene millennial climate oscillations. Geology 45 (4), 303–306.
Durán, L., Sánchez, E., Yagüe, C., 2013. Climatology of precipitation over the Iberian Central System mountain range. Int. J. Climatol. 33 (9), 2260–2273. https://doi.org/10.1002/joc.3602.
Eriksson, L., Johansson, E., Kettaneh-Wodl, N., Wold, S., 1999. Introduction to Multiand Megavariate Data Analysis Using Projection Methods (PCA & PLS). Umetrics AB, Umeå.
Fabián, J., Blanco-González, A., López-Sáez, J.A., 2006. La transición Calcolítico-Bronce Antiguo desde una perspectiva arqueológica y ambiental: el Valle Amblés (Ávila) como referencia. Arqueol. Espac. 26, 37–56.
Finsinger, W., Kelly, R., Fevre, J., Magyari, E.K., 2014. A guide to screening charcoal peaks in macro-charcoal-area records for fire-episode reconstructions. Holocene 24, 1002–1008. https://doi.org/10.1177/0959683614534737.
Fisher, T.G., Smith, D.G., Andrews, J.T., 2002. Preboreal oscillation caused by a glacial Lake Agassiz flood. Quat. Sci. Rev. 21, 873–878. https://doi.org/10.1016/S0277-3791(01)00148-2.
Fitzgerald, E., Ault, A.P., Zauscher, M.D., Mayol-Bracero, O.L., Prather, K.A., 2015. Comparison of the mixing state of long-range transported Asian and African mineral dust. Atmos. Environ. 115, 19–25. https://doi.org/10.1016/j.atmosenv.2015.04.031.
Fia≥kiewicz-Kozie≥, B., Ko≥aczek, P., Michczyƞski, A., Piotrowska, N., 2015. The construction of a reliable absolute chronology for the last two millennia in an anthropogenically disturbed peat bog: Limitations and advantages of using a radio-isotopic proxy and age-depth modelling. Quaternary Geochronology, 25, pp. 83-95.
Fletcher, W.J., Sánchez-Goñi, M.F., Allen, J.R.M., Cheddadi, R., Cambourieu-Nebout, N., Huntley, B., Lawson, I., Londeix, L., Magri, D., Margari, V., Muller, U.C., Naughton, F., Novenko, E., Roucoux, K., Tzedakis, P.C., 2010. Millennial-scale variability during the last glacial in vegetation records from Europe. Quat. Sci. Rev. 29, 2839–2864. https://doi.org/10.1016/j.quascirev.2009.11.015.
Franco-Múgica, F., Antón, M.G., Ollero, H.S., 1998. Vegetation dynamics and human impact in the Sierra de Guadarrama, Central System, Spain. The Holocene 8, 69–82.
Gallego, J.L.R., Ortíz, J., Sierra, C., Torres, T., Llamas, J.F., 2013. Multivariate study of trace element distribution in the geological record of Roñanzas Peat Bog (Asturias, N. Spain). Paleoenvironmental evolution and human activities over the last 8000 cal yr BP. Sci. Total Environ. 454–455, 16–29.
Garcés-Pastor, S., Cañellas-Boltà, N., Clavaguera, A., Calero, M.A., Vegas, T., 2017. Vegetation shifts, human impact and peat bog development in Bassa Nera pond (Central Pyrenees) during the last millennium. The Holocene 27 (4), 553–565. https://doi.org/10.1177/0959683616670221.
García-Alix, A., Jiménez-Moreno, G., Jiménez-Espejo, F.J., García-García, F., Delgado Huertas, A., 2014. An environmental snapshot of the Bølling interstadial in Southern Iberia. Quat. Res. 81, 284–294. https://doi.org/10.1016/j.yqres.2014.01.009.

García-Álvarez, S., Bal, M.C., Allée, P., García-Amorena, I., Rubiales, J.M., 2017. Holocene treeline history of a high-mountain landscape inferred from soil charcoal: The case of Sierra de Gredos (Iberian Central System, SW Europe). Quat. Int. 457, 85–98. https://doi.org/10.1016/j.quaint.2017.04.019.

García-Ruiz, J.M., Palacios, D., González-Sampériz, P., de Andrés, N., Moreno, A., Valero-Garcés, B., Gómez-Villar, A., 2016. Mountain glacier evolution in the Iberian Peninsula during the Younger Dryas. Quat. Sci. Rev. 138, 26–30. https://doi.org/10.1016/j.quascirev.2016.02.022.

González-Sampériz, P., Gil-Romera, G., García-Prieto, E., Aranbarri, J., Moreno, A., Morellón, M., Sevilla-Callejo, M., Leunda, M., Santos, L., Franco-Múgica, F., Andrade, A., Carrión, J.S., Valero-Garcés, B.L., 2020. Strong continentality and effective moisture drove unforeseen vegetation dynamics since the last interglacial at inland Mediterranean areas: The Villarquemado sequence in NE Iberia. Quat. Sci. Rev. 242, 106425 https://doi.org/10.1016/j.quascirev.2020.106425.

González-Sampériz, P., Leroy, S.A.G., Carrión, J.S., Fernández, S., García-Antón, M., Gil-García, M.J., Uzquiano, P., Valero-Garcés, B., Figueiral, I., 2010. Steppes, savannahs, forests and phytodiversity reservoirs during the Pleistocene in the Iberian Peninsula. Rev. Palaeobot. Palynol. 162, 427–457. https://doi.org/10.1016/j.revpalbo.2010.03.009.

González-Sampériz, P., Valero-Garcés, B.L., Moreno, A., Jalut, G., García-Ruiz, J.M., Martí-Bono, C.E., Delgado-Huertas, A., Navas, A., Otto, T., Dedoubat, J.J., 2006. Climate variability in the Spanish Pyrenees during the last 30,000 yr revealed by the El Portalet sequence. Quat. Res. 66, 38–52. https://doi.org/10.1016/j.yqres.2006.02.004.

Grousset, F.E., Biscaye, P.E., 2005. Tracing dust sources and transport patterns using Sr. Nd and Pb isotopes: Chemical Geology 222, 149–167. https://doi:10.1016/j.chemgeo.2005.05.006.

Haliuc, A., Veres, D., Brauer, A., Hubay, K., Hutchinson, S.M., Begy, R., Braun, M., 2017. Palaeohydrological changes during the mid and late Holocene in the Carpathian area, central-eastern Europe. Glob. Planet. Change 152, 99–114. https://doi.org/10.1016/j.gloplacha.2017.02.010.

Hammer, Ø., Harper, D.A.T., Ryan, P.D., 2001. Palaeontological statistics software package for education and data analysis. Palaeontol. Electron. 4, 1–9 https://doi.org/palaeo-electronica.org/2001_1/past/issue1_01.

Heiri, O., Lotter, A.F., Lemacke, G., 2001. Loss-on-ignition for estimating organic and carbonate content in sediments: reproducibility and comparability of results. J. Palaeolimnol. 25, 101–110. https://doi.org/10.1023/A:1008119611481.

Höbig, N., Weber, M.E., Kehl, M., Weniger, G.C., Julià, R., Melles, M., Fülöop, R.H., Vogel, H., Reicherter, K., 2012. Lake Banyoles (northeastern Spain): a Last Glacial to Holocene multi-proxy study with regard to environmental variability and human occupation. Quat. Int. 274, 205–218. https://doi.org/10.1016/j.quaint.2012.05.036.

Hodson, A., 2008. In: Phosphorus in glacial meltwaters. Blackwell Publishing Co., Oxford (UK), Glacier Science and Environmental Change, pp. 75–78.

Iriarte-Chiapusso, M.J., Muñoz-Sobrino, C., Gómez-Orellana, L., Hernández-Beloqui, B., García-Moreiras, I., Fernández-Rodríguez, C., Heiri, O., Lotter, A.F., Ramil-Rego, P., 2016. Reviewing the Lateglacial-Holocene transition in NW Iberia: A palaeoecological approach based on the comparison between dissimilar regions. Quat. Int. 403, 211–236. https://doi.org/10.1016/j.quaint.2015.09.029.

Jalut, G., Esteban-Amat, A., Bonnet, L., Gauquelin, T., Fontugne, M., 2000. Holocene climatic changes in the western Mediterranean, from south-east France to south-east Spain. Palaeogrography, Palaeoclimatology, Palaeoecology 160 (3), 255–290. https://doi.org/10.1016/S0031-0182(00)00075-4.

Jalut, G., Turu, V., Dedoubat, J.J., Otto, T., Ezquerra, J., Fontugne, M., Belet, J.M., Bonnet, L., de Celis, A.G., Redondo-Vega, J.M., Vidal-Romaní, J.R., Santos, L., 2010. Palaeoenvironmental studies in NW Iberia (Cantabrian range): vegetation history and synthetic approach of the last deglaciation phases in the Western Mediterranean. Palaeogeogr. Palaeoclimatol. Palaeoecol. 297, 330–350. https://doi.org/10.1016/j.palaeo.2010.08.012.

Keppler, F., Biester, H., 2003. Peatlands: a major sink of naturally formed organic chlorine. Chemosphere 52, 451–453. https://doi.org/10.1016/S0045-6535(03)00210-8.

Keppler, F., Biester, H., Putshew, A., Silk, P.J., Schöler, H.F., Müller, G., 2004. Organoiodine formation during humification in peatlands. Environ. Chem. Lett. 1, 219–223. https://doi.org/10.1007/s10311-003-0044-5.

Kjær H. A., Dallmayr R., Gabrieli J., Goto-Azuma K., Hirabayashi M., Svensson A. and Vallelonga, P., 2015. Greenland ice cores constrain glacial atmospheric fluxes of phosphorus. Journal of Geophysical Research: Atmospheres, 120 (20), 10.810-10.822.

Koinig, K., Shotyk, W., Lotter, A., Ohlendorf, C., 2003. 9000 years of geochemical evolution of lithogenic major and trace elements in the sediment of an alpine lake. J. Palaeolimnol. 4, 307–320. https://doi.org/10.1023/A:1026080712312.

Kobashi, T., Severinghaus, J.P., Barnola, J.M., 2008. 4 ± 1.5°C abrupt warming 11,270 yr ago identified from trapped air in Greenland ice. Earth Planet. Sci. Lett. 268, 397–407.

Ko≥aczek, P., Ga≥ka, M., Lamentowicz, M., Marcisz, K., Kajuka≥o-Drygalska, K., Karpińska- Ko≥aczek, M., 2018. Increased radiocarbon dating resolution of ombrotrophic peat profiles reveals periods of disturbance which were previously undetected. Quaternary Geochronology 52, 21-28.

Kylander, M.E., Ampel, L., Wohlfarth, B., Veres, D., 2011. High-resolution X-ray fluorescence core scanning analysis of Les Echets (France) sedimentary sequence: new insights from chemical proxies. J. Quat. Sci. 26, 109–117. https://doi.org/10.1002/jqs.1438.

Leri, A.C., Myneni, S.C.B., 2012. Natural organobromine in terrestrial ecosystems. Geochim. Cosmochim. Acta 77, 1–10. https://doi.org/10.1016/j.gca.2011.11.012.

Le Roux, G., Fagel, N., De Vleeschouwer, F., Krachler, M., Debaille, V., Stille, P., Mattielli, N., van der Knaap, W.O., van Leeuwen, J.F.N., Shotyk, W., 2012. Volcano- and climate-driven changes in atmospheric dust sources and fluxes since the Late Glacial in Central Europe. Geology 2012;; 40 (4): 335–338. doi: https://doi.org/10.1130/G32586.1.

Lillios, K.T., Blanco-González, A., Lee-Drake, B., López-Sáez, J.A., 2016. Mid-Late Holocene climate, demography, and cultural dynamics in Iberia: a multi-proxy approach. Quat. Sci. Rev. 135, 138–153. https://doi.org/10.1016/j.quascirev.2016.01.011.

López, P., Navarro, E., Marce, R., Ordóñez, J., Caputo, L., Armengol, J., 2006. Elemental ratios in sediments as indicators of ecological processes in Spanish reservoirs. Limnetica 25, 499–512.

López-Merino, L., Martínez-Cortizas, A., López-Sáez, J.A., 2010. Early agriculture and palaeoenvironmental history in the North of the Iberian Peninsula: a multi-proxy analysis of the Monte Areo mire (Asturias, Spain). J. Archaeol. Sci. 37, 1978–1988. https://doi.org/10.1016/j.jas.2010.03.003.

López-Merino, L., Martínez-Cortizas, A., López-Sáez, J.A., 2011. Human-induced changes on wetlands: a study case from NW Iberia. Quat. Sci. Rev. 30, 2745–2754. https://doi.org/10.1016/j.quascirev.2011.06.004.

López-Merino, L., Silva-Sánchez, N., Kaal, J., López-Sáez, J.A., Martínez-Cortizas, A., 2012. Post-disturbance vegetation dynamics during the Late Pleistocene and the Holocene: an example from NW Iberia. Glob. Planet. Change 92–93, 58–70. https://doi.org/10.1016/j.gloplacha.2012.04.003.

López-Sáez, J.A., López-Merino, L., Pérez-Díaz, S., 2008. Crisis climáticas en la Prehistoria de la Península Ibérica: el evento 8200 cal. BP como modelo. In: Rovira, S., García-Heras, M., Gener, M., Montero, I. (Eds.), VII Congreso Ibérico de Arqueometría. CSIC, Madrid, pp. 77–86.

López-Sáez, J.A., Blanco-González, A., López-Merino, L., Ruiz-Zapata, M.B., Dorado, M., Pérez-Díaz, S., Valdeolmillos, A., Burjachs, F., 2009. Landscape and climatic changes during the end of the Late Prehistory in the Amblés Valley (Ávila, central Spain), from 1200 to 400 cal BC. Quat. Int. 200, 90–101. https://doi.org/10.1016/j.quaint.2008.07.010.

López-Sáez, J.A., Abel-Schaad, D., Pérez-Díaz, S., Blanco-González, A., Alba-Sánchez, F., Dorado, M., Ruiz-Zapata, B., Gil-García, M.J., Gómez-González, C., Franco-Múgica, F., 2014. Vegetation history, climate and human impact in the Spanish Central System over the last 9,000 years. Quat. Int. 353, 98–122. https://doi.org/10.1016/j.quaint.2013.06.034.

López-Sáez, J.A., Abel-Schaad, D., Robles-López, S., Pérez-Díaz, S., Alba-Sánchez, F., Nieto-Lugilde, D., 2016. Landscape dynamics and human impact on high-mountain woodlands in the Western Spanish Central System during the last three millennia. J. Archaeol Sci. Rep. 9, 203–218. https://doi.org/10.1016/j.jasrep.2016.07.027.

López-Sáez, J.A., Figueiral, I., Cruz, D., 2017. Palaeoenvironement and vegetation dynamics in Serra da Nave (Alto Paiva, Beira Alta, Portugal) during the Late Pleistocene and the Holocene. Est. Pré-hist. 17, 11–23.

López-Sáez, J.A., Abel-Schaad, D., Luelmo-Lautenschlaeger, R., Robles-López, S., Pérez-Díaz, S., Alba-Sánchez, F., Sánchez-Mata, D., Gavilán, R.G., 2018a. Resilience, vulnerability and conservation strategies in high-mountain pine forests in the Gredos range, central Spain. Plant Ecol. Divers. 11, 97–110. https://doi.org/10.1080/17550874.2018.1449261.

López-Sáez, J.A., Vargas, G., Ruiz, J., Blarquez, O., Alba-Sánchez, F., Oliva, M., Pérez-Díaz, S., Robles-López, S., Abel-Schaad, D., 2018b. Palaeofire dynamics in central Spain during the late Holocene: The role of climatic and anthropogenic forcing. Land Degrad. Dev. 29, 2045–2059. https://doi.org/10.1002/ldr.2751.

López-Sáez, J.A., Carrasco, R.M., Turu, V., Ruiz-Zapata, B., Gil-García, M.J., Luelmo-Lautenschlaeger, R., Pérez-Díaz, S., Alba-Sánchez, F., Abel-Schaad, D., Ros, X., Pedraza, J., 2020. Late Glacial-early Holocene vegetation and environmental changes in the Western Iberian Central System inferred from a key site: The Navamuño record, Béjar range (Spain). Quat. Sci. Rev. 230, 106167 https://doi.org/10.1016/j.quascirev.2020.106167.

Mackereth, F.J.H., 1966. Some chemical observations on post-glacial lake sediments. Philos. Trans. R. Soc. Lond., B, Biol. Sci. 250 (765), 165–213. https://doi.org/10.1098/rstb.1966.0001.

Magny, M., Comborieu-Nebout, N., de Beaulieu, J.L., Bout-Roumazeilles, V., Colombaroli, D., Desprat, S., Francke, A., Joannin, S., Ortu, E., Peyron, O., Revel, M., Sadori, L., Siani, G., Sicre, M.A., Samartin, S., Simonneau, A., Tinner, W., Vannière, B., Wagner, B., Zanchetta, G., Anselmetti, F., Brugiapaglia, E., Chapron, E., Debret, M., Desmet, M., Didier, J., Essallami, L., Galop, D., Gilli, A., Haas, J.N., Kallel, N., Millet, L., Stock, A., Turon, J.L., Wirth, S., 2013. North-south palaeohydrological contrasts in the central Mediterranean during the Holocene: tentative synthesis and working hypotheses. Clim. Past 9, 2043–2071. https://doi.org/10.5194/cp-9-2043-2013.

Martín-Puertas, C., Jiménez-Espejo, F., Martínez-Ruiz, F., Nieto-Moreno, V., Rodrigo, M., Mata, M.P., Valero-Garcés, B.L., 2011. Late Holocene climate variability in the southwestern Mediterranean region: an integrated marine and terrestrial geochemical approach. Clim. Past 6, 807–816. https://doi.org/10.5194/cp-6-807-2010.

Mateus, J.E. 1992. Holocene and present-day ecosystems of the Canalhal Region, Southwest Portugal. Phd Thesis, Utrecht University, 184 p.

McDermott, F., Mattey, D.P., Hawkesworth, C., 2001. Centennial-scale holocene climate variability revealed by a high-resolution speleothem delta O-18 record from SW Ireland. Science 294, 1328–1331.

Mesa-Fernández, J.M., Jiménez-Moreno, G., Rodrigo-Gámiz, M., García-Alix, A., Jiménez-Espejo, F.J., Martínez-Ruiz, F., Anderson, R.S., Camuera, J., Ramos-Román, M.J., 2018. Vegetation and geochemical responses to Holocene rapid climate change in the Sierra Nevada (southeastern Iberia): the Laguna Hondera record. Clim. Past 14, 1687–1706. https://doi.org/10.5194/cp-14-1687-2018.

Morales-Molino, C., García-Antón, M., Postigo-Mijarra, J.M., Morla, C., 2013. Holocene vegetation, fire and climate interactions on the westernmost fringe of the Mediterranean Basin. Quat. Sci. Rev. 59, 5–17. https://doi.org/10.1016/j.quascirev.2012.10.027.

Morellón, M., Aranbarri, J., Moreno, A., González-Sampériz, P., Valero-Garcés, B.L., 2018. Early Holocene humidity patterns in the Iberian Peninsula reconstructed from lake, pollen and speleothem records. Quat. Sci. Rev. 181, 1–18. https://doi.org/10.1016/j.quascirev.2017.11.016.

Morellón, M., Valero-Garcés, B., Vegas-Villarrúbia, T., González-Sampériz, P., Romero, O., Delgado-Huertas, A., Mata, P., Moreno, A., Rico, M., Corella, J.P., 2009. Lateglacial and Holocene palaeohydrology in the Western Mediterranean region: the Lake Estanya record (NE Spain). Quat. Sci. Rev. 28, 2582–2599. https://doi.org/10.1016/j.quascirev.2009.05.014.

Moreno, A., López-Merino, L., Leira, M., Marco-Barba, J., González Sampériz, P., Valero Garcés, B., López-Sáez, J.A., Santos, L., Mata, P., Ito, E., 2011. Revealing the last 13,500 years of environmental history from the multiproxy record of a mountain lake (Lago Enol, northern Iberian Peninsula). J. Palaeolimnol. 46, 327–349. https://doi.org/10.1007/s10933-009-9387-7.

Moreno, A., Svensson, A., Brooks, S.K., Connor, S., Engels, S., Fletcher, W., Genty, D., Heiri, O., Labuhn, I., Persoiu, A., Peyron, O., Sadori, L., Valero-Garcés, B.L., Wulf, S., Zanchetta, G., 2014. A compilation of Western European terrestrial records 60–8 ka BP: towards an understanding of latitudinal climatic gradients. Quat. Sci. Rev. 106, 167–185. https://doi.org/10.1016/j.quascirev.2014.06.030.

Muñoz-Sobrino, C., Heiri, O., Hazekamp, M., van der Velden, D., Kirilova, E.P., García-Moreiras, I., Lotter, A.F., 2013. New data on the Lateglacial period of SW Europe: a high resolution multiproxy record from Laguna de la Roya (NW Iberia). Quat. Sci. Rev. 80, 58–77. https://doi.org/10.1016/j.quascirev.2013.08.016.

Muñoz-Sobrino, C., Ramil-Rego, P., Gómez-Orellana, L., 2004. Vegetation of the Lago de Sanabria area (NW Iberia) since the end of the Pleistocene: a palaeoecological reconstruction on the basis of two new pollen sequences. Veg. Hist. Archaeobotany 13, 1–22. https://doi.org/10.1007/s00334-003-0028-1.

Naeher, S., Gilli, A., North, R.P., Hamann, Y., Schubert, C.J., 2013. Tracing bottom water oxygenation with sedimentary Mn/Fe ratios in Lake Zurich. Switzerland. Chem. Geol. 352, 125–133. https://doi.org/10.1016/j.chemgeo.2013.06.006.

Naughton, F., Costas, S., Gomes, S.D., Desprat, S., Rodrigues, T., Sánchez-Goñi, M.F., Renssen, H., Trigo, R., Bronk-Ramsey, C., Oliveira, D., Salgueiro, E., Voelker, A.H.L., Abrantes, F., 2019. Coupled ocean and atmospheric changes during Greenland stadial 1 in southwestern Europe. Quat. Sci. Rev. 212, 108–120. https://doi.org/10.1016/j.quascirev.2019.03.033.

Naughton, F., Sanchez-Goñi, M.F., Desprat, S., Turon, J.L., Duprat, J., Malaize, B., Joli, C., Cortijo, E., Drago, T., Freitas, M.C., 2007. Present-day and past (last 25 000 years) marine pollen signal off Western Iberia. Mar. Micropalaeontol. 62, 91–114. https://doi.org/10.1016/j.marmicro.2006.07.006.

Oliva, M., Ruiz-Fernández, J., Barriendos, M., Benito, G., Cuadrat, J.M., Domínguez-Castro, F., García-Ruiz, J.M., Giralt, S., Gómez-Ortiz, A., Hernández, A., López-Costas, O., López-Moreno, J.I., López-Sáez, J.A., Martínez-Cortizas, A., Moreno, A., Prohom, M., Saz, M.A., Serrano, E., Tejedor, E., Trigo, R., Valero-Garcés, B., Vicente, S.M., 2017. The Little Ice Age in Iberian mountains. Earth-Sci. Rev. 177, 175–208. https://doi.org/10.1016/j.earscirev.2017.11.010.

Oliva-Urcía, B., et al., 2018. Last deglaciation and Holocene environmental change at high altitude in the Pyrenees: the geochemical and palaeomagnetic record from Marboré Lake (N Spain). J. Palaeolimnol. 59, 349–371. https://doi.org/10.1007/s10933-017-0013-9.

Oppenheimer, C., 2003. Climatic, environmental and human consequences of the largest known historic eruption: Tambora volcano (Indonseia) 1815. Progress in Physical Geography: Earth and Environment 27 (2), 230–259. https://doi.org/10.1191/0309133303 pp3379a.

Palacios, D., de Andrés, N., Gómez-Ortiz, A., García-Ruiz, J.M., 2016. Evidence of glacial activity during the Oldest Dryas in the mountains of Spain. In: Hughes, P.M., Woodward, J.C. (Eds.), Quaternary Glaciation in the Mediterranean Mountains. Geological Society Special Publications 433, London, pp. 87–110.

Pedraza, J., 1994. Geomorfología del Sistema Central. In: Gutiérrez-Elorza, M. (Ed.), Geomorfología de España. Editorial Rueda, Madrid, pp. 63–100.

Pedraza, J., Carrasco, R.M., Domínguez-Villar, D., Villa, J., 2013. Late Pleistocene glacial evolutionary stages in the Gredos Mountains (Iberian Central System). Quat. Int. 302, 88–100. https://doi.org/10.1016/j.quaint.2012.10.038.

Pèlachs, A., Julià, R., Pérez-Obiol, R., Soriano, J.M., Bal, M.C., Cunill, R., Catalán, J., 2011. Potential influence of Bond events on mid-Holocene climate and vegetation in southern Pyrenees as assessed from Burg lake LOI and pollen records. The Holocene 21 (1), 95–104. https://doi.org/10.1177/0959683610386820.

Pérez-Obiol, R., Jalut, G., Julia, R., Pèlachs, A., Iriarte, M.J., Otto, T., Hernandez-Beloqui, B., 2011. Mid-Holocene vegetation and climatic history of the Iberian Peninsula. The Holocene 21, 75–93.

Pérez-Obiol, R., García-Codron, J.C., Pèlachs, A., Pérez-Haase, A., Soriano, J.M., 2016. Landscape dynamics and fire activity since 6740 cal yr BP in the Cantabrian region (La Molina peat bog, Puente Viesgo, Spain). Quat. Sci. Rev. 135, 65–78. https://doi.org/10.1016/j.quascirev.2016.01.021.

Pérez-Mejías, C., Moreno, A., Bernal-Wormull, J., Cacho, I., Osácar, M.C., Edwards, R.L., Cheng, H., 2021. Oldest Dryas hydroclimate reorganisation in the eastern Iberian Peninsula after the iceberg discharges of Heinrich Event 1. Quat. Res. 101, 67–83. https://doi.org/10.1017/qua.2020.112.

Petisco de Lara, S.E. 1996. Caracterización de la circulación atmosferica en superfície y niveles altos en el área de la Península Ibérica y Baleares. Instututo Nacional de Méteorologia. Servicio de análisis e investigación del clima (Spain). 11, 69 pp.

Peyron, O., Bégeot, C., Brewer, S., Heiri, O., Magny, M., Millet, L., Ruffaldi, P., Van Campo, E., Yu, G., 2005. Late-Glacial climatic changes in Eastern France (Lake Lautrey) from pollen, lake-levels, and chironomids. Quat. Res. 64, 197–211. https://doi.org/10.1016/j.yqres.2005.01.006.

Poblete-Piedrabuena, M.A., Martí Molist, J., Beato Bergua, S., Marino Alfonso, J.L., 2019. Geomorphological evolution and chronology of the eruptive activity of the Columba and Cuevas volcanoes (Campo de Calatrava Volcanic Field, Ciudad Real, Central Spain). Geomorphology 335, 52–64.

Pontevedra-Pombal, X., Castro, D., Carballeira, R., Souto, M., López-Sáez, J.A., Pérez-Díaz, S., Fraga, M.I., Valcárcel, M., García-Rodeja, E., 2017. Iberian acid peatlands: types, origin and general trends of development. Mires Peat 19, 1–19. https://doi.org/10.19189/MaP.2016.OMB.260.

Pontevedra-Pombal, X., Castro, D., Souto, M., Fraga, M.I., Blake, W., Blaauw, M., López-Sáez, J.A., Pérez-Díaz, S., Valcárcel, M., García-Rodeja, E., 2019. 10,000 years of climate control over carbon accumulation in an Iberian bog (southwestern Europe). Geosci. Front. 10, 1521–1533. https://doi.org/10.1016/j.gsf.2018.09.014.

Railsback, L.B., Liang, F., Vidal Romaí, J.R., Grandal-d'Anglade, A., Vaqueiro Rodríguez, M., Santos Fidalgo, L., Fernández Mosquera, D., Cheng, H., Edwards, R. L., 2011. Petrographic and isotopic evidence for Holocene long-term climate change and shorter-term environmental shifts from a stalagmite from the Serra do Courel of northwestern Spain, and implications for climatic history across Europe and the Mediterranean. Palaeogeogr. Palaeoclimatol. Palaeoecol. 305, 172–184.

Rasmussen, S.O., Seierstad, I.K., Andersen, K.K., Bigler, M., Dahl-Jensen, D., Johnsen, S. J., 2008. Synchronization of the NGRIP, GRIP, and GISP2 ice cores across MIS 2 and palaeoclimatic implications. Quat. Sci. Rev. 27, 18–28. https://doi.org/10.1016/j.quascirev.2007.01.016.

Rasmussen, S.O., Bigler, M., Blockley, S.P., Blunier, T., Buchardt, S.L., Clausen, H.B., Cvijanovic, I., Dahl-Jensen, D., Johnsen, S.J., Fischer, H., Gkinis, V., Guillevic, M., Hoek, W.Z., Lowe, J.J., Pedro, J.B., Popp, T., Seierstad, I.K., Steffensen, J.P., Svensson, A.M., Vallelonga, P., Vinther, B.M., Walker, M.J., Wheatley, J.J., Winstrup, M., 2014. A stratigraphic framework for abrupt climatic changes during the Last Glacial period based on three synchronized Greenland ice-core records: refining and extending the INTIMATE event stratigraphy. Quat. Sci. Rev. 106, 14–28. https://doi.org/10.1016/j.quascirev.2014.09.007.

Reimer, P.J., Bard, E., Bayliss, A., Beck, J.W., Blackwell, P.G., Bronk Ramsey, C., Buck, C. E., Cheng, H., Edwards, R.L., Friedrich, M., Grootes, P.M., Guilderson, T.P., Haflidason, H., Hajdas, I., Hatté, C., Heaton, T.J., Hoffmann, D.L., Hogg, A.G., Hughen, K.A., Kaiser, K.F., Kromer, B., Manning, S.W., Niu, M., Reimer, R.W., Richards, D.A., Scott, E.M., Southon, J.R., Staff, R.A., Turney, C.S.M., van der Plicht, J., 2013. Intcal13 and marine13 radiocarbon age calibration curves 0–50,000 years cal yr BP. Radiocarbon 55, 1869–1887. https://doi.org/10.2458/azu_js_rc.55.16947.

Renssen, H., Isarin, R.F.B., Vanderberghe, J., Workshop participants, 2010. Rapid climatic warming at the end of the last glacial: new perspectives. Glob. Planet. Change 30, 155–165. https://doi.org/10.1016/S0921-8181(01)00083-2.

Riera, S., Turu, V., 2011. Cambios en el paisaje del valle de Ordino al início del Holoceno: Evolución geomorfológica, paleovegetal e incendios de epoca Mesolítica (NW del Principado de Andorra, Pirineos Orientales). In: Turu, V., Constante, A. (Eds.), El Cuaternario en España y áreas afines, avances en 2011. AEQUA-Fundació Marcel Chevalier, Andorra la Vella, pp. 201–204.

Richter, T.O., Van der Gaast, S.J., Koster, B., Vaars, A., Gieles, R., De Stigter, H.C., de Haas, H., Van Weering, T.C.E., 2006. The Avaatech XRF core scanner: technical description and applications to NE Atlantic sediments. In: Society, L.G. (Ed.), New Techniques in Sediment Core Analysis. Geological Society of London (Special Publications), London, pp. 39–50.

Rius, D., Vannière, B., Galop, D., Richard, H., 2011. Holocene fire regime changes from multiple-site sedimentary charcoal analyses in the Lourdes basin (Pyrenees, France). Quat. Sci. Rev. 30, 1696–1709.

Roberts, C.N., Stevenson, T., Davis, B., Cheddadi, R., Brewster, S., Rosen, A., 2004. Holocene climate, environment and cultural change in the circum-Mediterranean region. In: Battarbee, R.W., Gasse, F., Stickley, C.E. (Eds.), Past climate variability through Europe and Africa. Springer, Dordrecht, pp. 343–362.

Rodrigo-Gámiz, M., Martínez-Ruiz, F., Jiménez-Espejo, F.J., Gallego-Torres, D., Nieto-Moreno, V., Romero, O., Ariztegui, D., 2011. Impact of climate variability in the Western Mediterranean during the last 20,000 years: oceanic and atmospheric responses. Quat. Sci. Rev. 30, 2018–2034. https://doi.org/10.1016/j.quascirev.2011.05.011.

Rubiales, J.M., García-Amorena, I., Génova, M., Gómez Manzaneque, F., Morla, C., 2007. The Holocene history of highland pine forests in a submediterranean mountain: the case of Gredos mountain range (Iberian Central range, Spain). Quat. Sci. Rev. 26, 1759–1770.

Ruiz-Fernández, J., Oliva, M., Cruces, A., Lopes, V., Freitas, M.C., Andrade, C., García-Hernández, C., López-Sáez, J.A., Geraldes, M., 2016. Environmental evolution in the Picos de Europa (Cantabrian Mountains, SW Europe) since the Last Glaciation. Quat. Sci. Rev. 138, 87–104. https://doi.org/10.1016/j.quascirev.2016.03.002.

Sánchez-López, G., Hernández, A., Pla-Rabes, S., Trigo, R.M., Toro, M., Granados, I., Sáez, A., Masqué, P., Pueyo, J.J., Rubio-Inglés, M.-J., Giralt, S., 2016. Climate reconstruction for the last two millennia in central Iberia: The role of East Atlantic (EA), North Atlantic Oscillation (NAO) and their interplay over the Iberian Peninsula. Quat. Sci. Rev. 149, 135–150. https://doi.org/10.1016/j.quascirev.2016.07.021.

Sadori, L., 2018. The Lateglacial and Holocene vegetation and climate history of Lago di Mezzano (central Italy). Quat. Sci. Rev. 202, 30–44. https://doi.org/10.1016/j.quascirev.2018.09.004.

Santos-Fidalgo, L., Vidal-Romaní, J.R., Jalut, G., 2000. History of vegetation during the Holocene in the Courel and Queixa Sierras. Galicia, northwest Iberian Peninsula, Journal of Quaternary Science 15 (6), 621–632.

Schaller, T., Christoph Moor, H., Wehrli, B., 1997. Sedimentary profiles of Fe, Mn, V, Cr, As and Mo as indicators of benthic redox conditions in Baldeggersee. Aquat. Sci. 59, 345–361. https://doi.org/10.1007/BF02522363.

Schofield, J.E., Edwards, K.J., Mighall, T., Martínez-Cortizas, A., Rodríguez-Racedo, J., Cook, G., 2010. An integrated geochemical and palynological stude of human impacts, soil erosion and storminess from southern Greenland since c. AD 1000. Palaeogeogr. Palaeoclimatol. Palaeoecol. 295, 19–30. https://doi.org/10.1016/j.palaeo.2010.05.011.

Schröder, T., van't Hoff, J., López-Sáez, J.A., Viehberg, F., Melles, M., Reicherter, K., 2018. Holocene climatic and environmental evolution on the southwestern Iberian Peninsula: A high-resolution multi-proxy study from Lake Medina (Cádiz, SW Spain). Quat. Sci. Rev. 198, 208–225. https://doi.org/10.1016/j.quascirev.2018.08.030.

Silva-Sánchez, N., Martínez-Cortizas, A., Abel-Schaad, D., López-Sáez, J.A., Mighall, T. M., 2016. Influence of climate change and human activities in the organic and inorganic composition of peat during the Little Ice Age (El Payo mire, Gata range, W Spain). Holocene 26, 1290–1303. https://doi.org/10.1177/0959683616638439.

Taboada, T., Martínez-Cortizas, A., García, C., García-Rodeja, E., 2006. Particle-size fractionation of titanium and zirconium during weathering and pedogenesis of granitic rocks in NW Spain. Geoderma 131, 218–236. https://doi.org/10.1016/j.geoderma.2005.03.025.

Tarroso, P., Carrión, J.S., Dorado, M., Queiroz, P., Santos, L., Valdeolmillos, A., Alves, P. C., Brito, J.C., Cheddadi, R., 2016. Spatial climate dynamics in the Iberian Peninsula since 15 000 years. Clim. Past 12, 1137–1149. https://doi.org/10.5194/cp-12-1137-2016.

Thompson, R., Oldfield, F., 1986. Environmental magnetism. Springer, Dordrecht. https://doi.org/10.1007/978-94-011-8036-8.

Tomasso, A., Cheung, C.F., Fornage-Bontemps, S., Langlais, M., Naudinot, N., 2018. Winter is coming: What happened in western European mountains between 12.9 and 12.6 ka cal. BP (beginning of the GS1). Quat. Int. 465, 210–221. https://doi.org/10.1016/j.quaint.2017.12.020.

Turney, C.S.M., Coope, G.R., Harkness, D.D., Lowe, J.J., Walker, M.J.C., 2000. Implications for the dating of Wisconsinan (Weichselian) Late-Weichselian events of systematic radiocarbon age differences between terrestrial plant macrofossils from a site in SW Ireland. Quat. Res. 53, 114–121.

Turu, V., Boulton, G.S., Ros, X., Peña-Monné, J.L., Martí-Bono, C., Bordonau, J., Serrano-Cañadas, E., Sancho-Marcén, C., Constante-Orrios, A., Pous, J., Gonzàlez-Trueba, J. J., Palomar, J., Herrero-Simón, R., Garcia-Ruiz, J.M., 2007. Structure des grands bassins glaciaires dans le nord de la Péninsule Ibérique: comparaison entre les vallées d'Andorre (Pyrénées Orientales), du Gállego (Pyrénées Centrales) et du Trueba (Chaîne Cantabrique). Quaternaire 18 (4), 309–325. https://doi.org/10.4000/quaternaire.1167.

Turu, V., Bordonau, J., 2013. Estudio geoquímico de los sedimentos glaciolacustres de La Massana y Ordino (Andorra, Pirineos Orientales): influjo sedimentario entre lagos de obturación yuxtaglaciar e interpretación paleoambiental. In: Baena, R., Fernandez, , J.J., and Guerrero, I., (Eds) El Cuaternario Ibérico: Investigación en el siglo XXI. Asociación Española para el Estudio del Cuaternario & Grupo do Trebalho Portugués para ou Estudio do Quaternario (AEQUA-GTPEQ), Sevilla – La Rinconada, 204 – 208.

Turu, V., Calvet, M., Bordonau, J., Gunnell, Y., Delmas, M., Vilaplana, J M., Jalut, G., 2017. Did Pyrenean glaciers dance to the beat of global climatic events? Evidence from the Würmian sequence stratigraphy of an ice-dammed palaeolake depocentre in Andorra. In Hughes, P. D., Woodward, J. C., (Eds.). Quaternary Glaciation in the Mediterranean Mountains. Geological Society, London, Special Publications. 433(1), 111-136. https://doi.org/10.1144/SP433.6.

Turu, V., Carrasco, R.M., Pedraza, J., Ros, X., Ruiz-Zapata, B., Soriano-López, J.M., Mur-Cacuho, E., Pèlachs-Mañosa, A., Muñoz-Martín, A., Sánchez, J., Echeverria-Moreno, A., 2018. Late glacial and post-glacial deposits of the Navamuño peatbog (Iberian Central System): Chronology and palaeoenvironmental implications. Quat. Int. 470, 82–95. https://doi.org/10.1016/j.quaint.2017.08.018.

Turu. V., 2018. High Resolution Chronostratigraphy from an Ice-Dammed Palaeo-Lake in Andorra: MIS 2 Atlantic and Mediterranean Palaeo-Climate Inferences over the SE Pyrenees. In: Aliello, G. (Ed.), New Insights into the Stratigraphic Setting of Paleozoic to Miocene Deposits-Case Studies from the Persian Gulf, Peninsular Malaysia and South-Eastern Pyrenees. IntechOpen. London, pp 63-81. https://doi.org/10.5772/intechopen.81395.

van der Knaap, W.O., van Leeuwen, J.F.N., 1994. Holocene vegetation, human impact, and climatic change in Serra da Estrela. Portugal. Diss. Bot. 234, 497–535. https://doi.org/10.7892/boris.81078.

van der Knaap, W.O., van Leeuwen, J.F.N., 1995. Holocene vegetation and degradation as responses to climatic change and human activity in the Serra da Estrela. Portugal. Rev. Palaeobot. Palynol. 89, 153–211. https://doi.org/10.1016/0034-6667(95)00048-0.

van der Knaap, W.O., van Leeuwen, J.F.N., 1997. Late Glacial and early Holocene vegetation sucession, altitudinal vegetation zonation, and climatic change in the Serra da Estrela. Portugal. Rev. Palaeobot. Palynol. 97, 239–285. https://doi.org/10.1016/S0034-6667(97)00008-0.

Van Pee, K.H., Unversuch, S., 2003. Biological dehalogenation and halogenation reactions. Chemosphere 52, 299–312. https://doi.org/10.1016/S0045-6535(03)00204-2.

Vannière, B., Power, M.J., Roberts, N., Tinner, W., Carrión, J.S., Magny, M., Bartlein, P., Colombaroli, D., Daniau, A.L., Finsinger, W., Gil-Romera, G., Kaltenrieder, P., Magri, D., Pini, R., Sadori, L., Turner, R., Valsechi, V., Vescovi, E., 2011. Circum-Mediterranean fire activity and climate changes during the mid-Holocene environmental transition (8500–2500 cal. BP). Holocene 21, 53–73. https://doi.org/10.1177/0959683610384164.

Vieira, G., Palacios, D., Andrés, N., Mora, C., Selem, L.V., Woronko, B., Soncco, C., Úbeda, J., Goyanes, G., 2021. Penultimate Glacial Cycle marks the maximum glacier extent in the Iberian Peninsula: New evidence from the Serra da Estrela (Central System, Portugal). Geomorphology 107781. https://doi.org/10.1016/j.geomorph.2021/107781.

Walczak, I.W., Baldini, J.U., Baldini, L.M., McDermott, F., Marsden, S., Standish, C.D., Richards, D.A., Andreo, B., Slater, J., 2015. Reconstructing high-resolution climate using CT scanning of unsectioned stalagmites: A case study identifying the mid-Holocene onset of the Mediterranean climate in southern Iberia. Quat. Sci. Rev. 127, 117–128.

Watts, W.A., Allen, J.R.M., Huntley, B., 1996. Vegetation history and palaeoclimate of the last glacial period at Lago Grande di Monticchio, southern Italy. Quat. Sci. Rev. 15, 133–153. https://doi.org/10.1016/0277-3791(95)00093-3.

Wei, D., González-Sampériz, P., Gil-Romera, G., Harrison, S.P., Prentice, I.C., 2019. Climate changes in interior semi-arid Spain from the last interglacial to the late Holocene. Climate Past Discuss. https://doi.org/10.5194/cp-2019-16.

Williams, C., Flower, B.P., Hastings, D.W., 2012. Seasonal Laurentide ice sheet melting during the 'Mystery Interval' (15.5–14.5 ka). Geology 40, 955–958. https://doi.org/10.1130/G33279.1.

Yu, Z., Eicher, U., 2001. Three amphi-Atlantic century-scale cold events during the Bølling-Allerød warm period. Géogr. Phys. Quatern. 55, 171–179. https://doi.org/10.7202/008301ar.

Zielhofer, C., Fletcher, W.J., Mischke, S., De Batist, M., Campbell, J.F.E., Joannin, S., Tjallingii, R., El Hamouti, N., Junginger, A., Stele, A., Bussmann, J., Schneider, B., Lauer, T., Spitzer, K., Strupler, M., Brachert, M., Brachert, T., Mikdad, A., 2017a. Atlantic forcing of western Mediterranean winter rain minima during the last 12,000 years. Quat. Sci. Rev. 157, 29–51. https://doi.org/10.1016/j.quascirev.2016.11.037.

Zielhofer, C., Suchodoletz, H., Fletcher, W.J., Schneider, B., Dietze, E., Schlegel, M., Schpanski, K., Weninger, B., MIschke, S., Mikdad, A., 2017b. Millennial-scale fluctuations in Saharan dust supply across the decline of the African Humid Period. Quat. Sci. Rev. 171, 119–135. https://doi.org/10.1016/j.quascirev.2017.07.010.